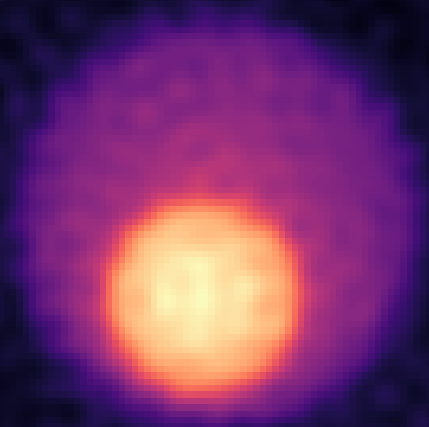


# A Study of 2D Refractive Index Reconstruction in Optical Diffraction Tomography

Bernd-Roland Marcus Rijn





# A Study of 2D Refractive Index Reconstruction in Optical Diffraction Tomography

by

Bernd-Roland Marcus Rijn

to obtain the degree of Bachelor of Science  
at the Delft University of Technology,  
to be defended publicly on Wednesday July 12, 2023 at 1:30 PM.

Student number: 5392098  
Project duration: April 24, 2023 – July 4, 2023  
Thesis committee: Dr. J. Kalkman, TU Delft, overall supervisor  
Dr. A. Yolalmaz, TU Delft, daily supervisor  
Dr. K. W. A. van Dongen, TU Delft

# Abstract

The imaging of biological cells needs to be optimal to study human diseases more effectively. This thesis discusses implementing multiple forward and reconstruction techniques and their performance, which is all done in a 2D quantitative study. The forward models are based on the Mie scattering theory and the split-step non-paraxial (SSNP) method. Mie scattering is based on the multipole expansions of the total complex field. The SSNP method is a sequential solver of the inhomogeneous Helmholtz equation. For the reconstruction, the Fourier diffraction theorem (FDT) is used with sample rotation (OR) and illumination scanning (LA) methods as different implementations of this theory. The FDT samples the complex field at semi-circular arcs, which is then interpolated on a rectangular grid using the *scipy.intp.griddata*-function. An inverse Fourier transform is performed to obtain the refractive index. The SSNP method is also used as a reconstruction method with an optimization equation using both the intensity and phase. The optimization equation is solved with the stochastic gradient descent (SGD) method, and the gradient is computed using automatic differentiation with the *TensorFlow*-package. The FDT method showed fast convergence to the ground truth solution for low contrast scatterers  $n_r \leq 1.01$ , but failed for multiple scatterers. The SSNP method showed convergence for every refractive index, however, the implementation is computationally heavy. For further research, implementing the methods in 3D and reducing the computational complexity is recommended by introducing a learning algorithm for the SSNP method.

# Contents

<b>Abstract</b>	<b>ii</b>
<b>1 Introduction</b>	<b>1</b>
<b>2 Theory of Optical Diffraction Tomography</b>	<b>4</b>
2.1 The Forward Models . . . . .	4
2.1.1 Analytical Scattering Calculation . . . . .	4
2.1.2 The Forward SSNP Method . . . . .	6
2.2 The Inverse Problem . . . . .	8
2.2.1 The Fourier Diffraction Theorem . . . . .	8
2.2.2 SSNP-based Tomographic Reconstruction . . . . .	12
<b>3 Methods</b>	<b>14</b>
3.1 Implementation . . . . .	14
3.2 Data Analysis . . . . .	15
<b>4 Results</b>	<b>17</b>
4.1 The Forward Scattering Problem . . . . .	17
4.1.1 The Exact Field against the Born Approximation . . . . .	17
4.1.2 The Forward SSNP Method . . . . .	19
4.2 The Inverse Problem . . . . .	20
4.2.1 Fourier Refractive Index Reconstruction under the Born Approximation . . . . .	21
4.2.2 Iterative Reconstruction with the SSNP Model . . . . .	23
<b>5 Discussion</b>	<b>30</b>
5.1 The Forward Scattering Problem . . . . .	30
5.2 The Inverse Problem . . . . .	31
5.2.1 Fourier Refractive Index Reconstruction under the Born Approximation . . . . .	31
5.2.2 Iterative Reconstruction with the SSNP Model . . . . .	32
<b>6 Conclusion</b>	<b>35</b>
<b>Bibliography</b>	<b>37</b>
<b>A Appendix</b>	<b>41</b>



# 1

## Introduction

To study human diseases, imaging biological cells plays a crucial role [1]. Traditional imaging techniques have their limitations, such as ionizing radiations, which damage living cells [2], limited contrast, and limited resolution [3]. The live imaging of biological cells in two- (2D) or three-dimensions (3D) holds tremendous potential for advancing the study of diseases [4]. This could be realized by introducing new reconstruction techniques such as optical diffraction tomography (ODT).

X-ray computed tomography (CT) uses X-rays as incoming waves with almost no scattering due to their short wavelength and high energy, which make them penetrate through dense materials such as bones. The typical spatial resolution is in the range of a few hundred micrometers [5]. X-ray CT has limited applicability for imaging biological cells since the absorption of those cells is too low, and the resolution is limited. Furthermore, X-ray scanning can damage biological cells. [2].

ODT is the optical equivalent of X-ray computed tomography, except that it uses visible light instead of X-rays [6]. It is a 2D and 3D reconstruction technique used to obtain a biological cell's refractive index (RI) [7]. The downside of ODT is that the light gets scattered, which increases the complexity of the wave propagation and hence results in a more complicated tomographic reconstruction. Since ODT uses visible light, the object is not damaged, which is the case for X-rays. The RI of a transparent object is an optical property used to describe the diffraction of light that propagates through the object [8]. The RI contains quantitative information about the structure and can describe the difference between different sub-cellular organelles, such as the cell-nucleolus [8]. Therefore, ODT can be used to study biological cells without using labels. The used sample size in ODT is typically in the range from a few micrometers to several millimeters. The resolution is typically in the range of a few hundred nanometers to a few micrometers [9], which is superior to the conventional X-ray CT.

The data-collection method is shown in Fig. 1.1. An incident plane wave propagates through a scattering object, resulting in a scattered outgoing wave measured at the detector for different angular projections.

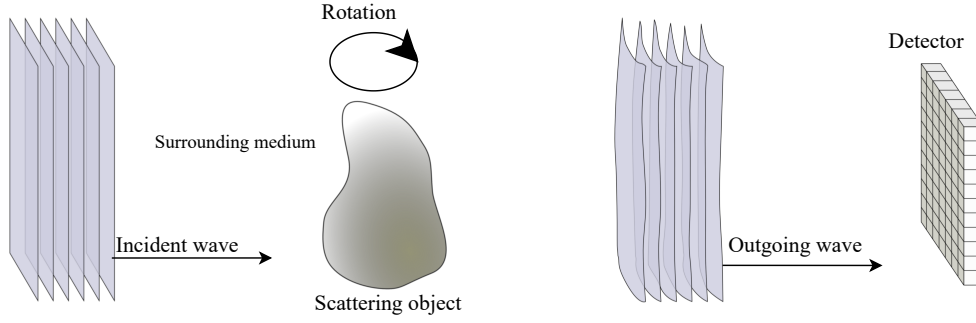


Figure 1.1: The data-collection method of the Fourier diffraction theorem. This is a modified figure from Müller [10].

Lately, multiple papers with different variants of ODT and intensity diffraction tomography (IDT) have been introduced. These techniques are based on reconstructing the refractive index (RI) based on the Fourier diffraction theorem (FDT) in Müller [10] and the split-step non-paraxial (SSNP) method in Zhu et al. [11].

The FDT is used to quantify the refractive index from several angular projections using the Born approximation, which only incorporates single scattering of the object. The FDT uses the inhomogeneous Helmholtz equation together with the Born approximation as a basis for the reconstruction. The complex field on the detector gets projected on semi-circular arcs in Fourier space for every angular projection. The projections are shifted based on the angle of the incoming wave with respect to the detector and the object. In this thesis two methods are discussed: sample rotation (OR) and illumination scanning (LA). The OR method rotates the object for a full  $360^\circ$  resulting in a fully covered Ewald sphere. The LA method only moves the light source over a certain angle, resulting in shifted arcs in Fourier space. This leads to, potentially, a twice as big wavenumber range compared to the OR method, which could improve the resolution in the lateral direction by a factor of 2. However, the sampling grid does miss information at certain frequencies due to a limited angle coverage, better known as the missing cone artifact [12]. The RI is found by performing an inverse Fourier transform on the interpolated grid for both methods.

The biggest downside of the FDT is that it assumes single scattering via the Born approximation. Although this approximation reduces the complexity, the method only works for low contrast scatterers or low-index contrast objects. Biological cells usually have a refractive index between  $n = 1.360$  and  $n = 1.420$  [13]. Those differences are beyond the reach of the Born approximation, and therefore this method would fail to reconstruct biological cells accurately.

The SSNP method does not use the Born approximation, and hence can potentially reconstruct the RI accurately. This method does not use paraxial assumptions, and therefore it can account for diffraction. Furthermore, the SSNP method can handle a wide range of geometries and material properties, making it a flexible and versatile method. This method's downsides are that it is computationally complex, and the grid size limits the reconstruction accuracy.

The SSNP method uses the inhomogeneous Helmholtz equation as the basis for the reconstruction. The complex field is calculated at every slice sequentially by rewriting the inhomogeneous Helmholtz equation in a propagation and scattering matrix. The reconstruction is performed by including both the phase and intensity in an optimization equation and iteratively updating the RI using the gradient of the complex field.



In this thesis, the FDT method is introduced and implemented in 2D for both OR and LA. The SSNP method is also introduced and implemented in 2D but only for OR. The advantages and limitations of the methods are discussed based on their performance, such as computation time and reconstruction accuracy. The used forward model is the Mie scattering of a cylinder, which can compute the analytical solution of the complex field and both the Born and Rytov approximation.

This thesis starts with the theory of the forward and inverse methods, then the implementation in Python is discussed in the methodology. The forward and inverse models are presented and discussed in the results and discussion.

# 2

## Theory of Optical Diffraction Tomography

### 2.1. The Forward Models

To compute the complex two-dimensional (2D) field  $U(\mathbf{r})$  at position  $\mathbf{r}$ , the Mie scattering and Split-step non-paraxial (SSNP) models are used. The basis of both techniques lies in the inhomogeneous Helmholtz equation:

$$(\nabla^2 + k_m^2)U(\mathbf{r}) = V(\mathbf{r})U(\mathbf{r}), \quad (2.1)$$

with  $k_m$  the wavenumber of the surrounding medium,  $U(\mathbf{r})$  the total complex field and  $V(\mathbf{r})$  the scattering potential. The total complex field  $U(\mathbf{r})$  can then be rewritten into two parts, the incoming field  $U_0(\mathbf{r})$  and the scattered field  $U_s(\mathbf{r})$  such that

$$U(\mathbf{r}) = U_0(\mathbf{r}) + U_s(\mathbf{r}). \quad (2.2)$$

This section shows the theory of computing a complex field  $U$  at a detector at a certain distance and angle from the incoming wave. The next section discusses how this complex field is used to reconstruct the refractive index.

#### 2.1.1. Analytical Scattering Calculation

In principle, the scattering potential can be any refractive index distribution. Here, we choose to calculate the scattered field for a cylinder with constant refractive index  $n_{\text{cyl}}$  in a homogeneous background refractive index  $n_m$ , since the solution of this distribution can be derived analytically. The analytical solution of this distribution can be derived using the Mie scattering model. This exact solution is used as a reference for computing the field's error.

In the Mie scattering model, the scattering of a homogeneous cylinder with RI  $n_{\text{cyl}}$  in a homogeneous background RI  $n_m$  can be computed exact, which is discussed below based on Devaney [14]. When a scattering cylinder is centered at the origin, the scattering potential  $V(\mathbf{r})$  can be defined as

$$V(\mathbf{r}) = \begin{cases} k_m^2 [1 - n_r^2] & r \leq R_0, \\ 0 & r \geq R_0, \end{cases} \quad (2.3)$$

where  $R_0$  is the radius of the cylinder,  $n_r = \frac{n_{\text{cyl}}}{n_m}$  the relative refractive index and  $\mathbf{r} = (r, \phi)$  the polar coordinates of the cylinder. For a homogeneous cylinder with relative refractive index  $n_r$ , which is illuminated by an incident wavefield that propagates in the  $(x, z)$ -plane perpendicular to the cylinder axis, the field expansion takes the form

$$U(r) = \sum_{l=-\infty}^{\infty} a_l J_l(k_m n_r r) e^{il\phi}, \quad r \leq R_0, \quad (2.4)$$

and

$$U(r) = \sum_{l=-\infty}^{\infty} a_{0l} J_l(k_m r) e^{il\phi} + \sum_{l=-\infty}^{\infty} b_l H_l^+(k_m r) e^{il\phi}, \quad r \geq R_0, \quad (2.5)$$

where  $J_l(x)$  is the Bessel function of the first kind,  $H_l^+(x)$  the Hankel function of the first kind and  $a_{0l}$ ,  $a_l$  and  $b_l$  the multipole moments. In our implementation, the incoming wave is defined as a plane wave which has the benefit that it has an exact multipole expansion defined as

$$e^{i\mathbf{k}_m \cdot \mathbf{r}} = e^{ik_m r \cos \phi_0} = \sum_{l=-\infty}^{\infty} i^l J_l(k_m r) e^{il\phi_0}, \quad (2.6)$$

with  $\phi$  the incoming angle. Using both equations and requiring that both the solutions and radial derivatives are identical at the boundary, the multipole moment  $b_l$  is defined as

$$b_l = R_l a_{0l}, \quad (2.7)$$

with

$$R_l = \frac{n_r J_l(k_m R_0) J_l'(k_m n_r R_0) - J_l'(k_m R_0) J_l(k_m n_r R_0)}{J_l(k_m n_r R_0) H_l^{+'}(k_m R_0) - n_r J_l'(k_m n_r R_0) H_l^+(k_m R_0)}, \quad (2.8)$$

the reflection coefficient, which links the scattered field and the incoming field.  $J_l'$  and  $H_l^{+'}$  are the derivatives of, respectively, the first order Bessel and Hankel functions. Combining Eqs. 2.4 - 2.7 results in

$$b_l = i^l e^{-il\phi_0} R_l, \quad (2.9)$$

using this together with Eqs. 2.2 and 2.5 the exact scattered field  $U_s$  can be obtained

$$U_s(\mathbf{r}, \mathbf{s}_0) = \sum_{l=-\infty}^{\infty} i^l R_l H_l^+(k_m r) e^{il(\phi - \phi_0)}. \quad (2.10)$$

The exact scattered field  $U_s$  computes the field at a position  $\mathbf{r}$  with multiple scattering included. However, the Born approximation is needed in the upcoming sections since this reduces the multiple scattering problem to a single scattering problem. The Born approximation is defined as

$$U^{(B)}(\mathbf{r}) = U_0(\mathbf{r}) + \iint d^2 r' G_{0+}(\mathbf{r} - \mathbf{r}') V(\mathbf{r}') U_0(\mathbf{r}), \quad (2.11)$$

with  $G_{0+}(\mathbf{r} - \mathbf{r}')$  the Green function. Because the Born approximation is only computed from the incoming field and not the scattered field, the complexity of the problem is reduced. The Green function is defined as the solution of

$$(\nabla^2 + k_m^2) G_{0+}(\mathbf{r} - \mathbf{r}') = \delta(\mathbf{r} - \mathbf{r}'), \quad (2.12)$$

with  $\delta(\mathbf{r} - \mathbf{r}')$  the delta peak. For the 2D-case  $G_{0+}(\mathbf{r} - \mathbf{r}')$  is proportional to the zero-order Hankel function of the first kind

$$G_{0+}(\mathbf{r} - \mathbf{r}') = -\frac{i}{4} H_0^{(1)}(k_m |\mathbf{r} - \mathbf{r}'|). \quad (2.13)$$

This is the starting point for the derivation of the single scattered field  $U_s^{(B)}$ . This scattered field can again be computed using the multipole expansion

$$U_s^{(B)}(\mathbf{r}) = -\frac{i}{4} \sum_{l=-\infty}^{\infty} q_l H_l^+(k_0 r) e^{il\phi}, \quad (2.14)$$

with the multipole moments  $q_l$  given by

$$q_l = \iint_{\tau_0} d^2 r V(r) U_0(r) J_l(k_0 r) e^{-il\phi} = \int_0^{R_0} \int_0^{2\pi} r dr d\phi V(r) U_0(r) J_l(k_0 r) e^{-il\phi}. \quad (2.15)$$

By implementing the incoming field defined in Eq. 2.6, the equation reduces to

$$q_l = 2\pi \int_0^{R_0} r dr V(r) J_l^2(k_0 r) a_{0l}. \quad (2.16)$$

The coefficients before the Hankel function in Eq. 2.14 can be grouped and written as a reflection coefficient multiplied by the coefficient of the incoming field, which is the same approach as with the exact field, such that

$$U_B(r) = \sum_{l=-\infty}^{\infty} R_l^{(B)} a_{0l} H_l^+(k_0 r) e^{il\phi}, \quad (2.17)$$

with

$$R_l^{(B)} = -i \frac{\pi}{2} \int_0^{R_0} r dr J_l^2(k_0 r) V(r) = -i \frac{\pi}{2} K_0^2 (1 - n_r^2) \mu_l^2(k_0 R_0). \quad (2.18)$$

and

$$\mu_l^2(k_0 R_0) = \int_0^{R_0} r dr J_l^2(k_0 r) = \frac{R_0^2}{2} [J_l^2(k_0 R_0) - J_{l-1}(k_0 R_0) J_{l+1}(k_0 R_0)]. \quad (2.19)$$

Since the Born approximation only deals with the single scattered field, this approximation is only valid when  $U_s \ll U_0$ .

Next to the Born approximation, the Rytov approximation can be used, which is defined as

$$U = e^{\phi_0 + \phi_1 + \phi_2 + \dots}, \quad (2.20)$$

by defining  $U_0 = e^{\phi_0}$  then the first Rytov approximation will be defined as

$$U_s^{(R)} = e^{\phi_1}, \quad (2.21)$$

which can also be written as a function of the Born approximation

$$U_s^{(R)} = U_i e^{\frac{U_s^{(B)}}{U_i}}, \quad (2.22)$$

which is just like the Born approximation, only valid for single scatterers. The Rytov approximation is generally more accurate than the Born approximation and has a greater domain of applicability [14].

Although, we will use the analytical solution as ground truth data, it is not very suitable for calculating the scattered field of an arbitrary scattering potential. For this, we use the SSNP method.

### 2.1.2. The Forward SSNP Method

The second method is the Split-Step Non-Paraxial (SSNP) method which is based on the work of Zhu et al. [11]. This method was initially designed for Intensity Diffraction Tomography (IDT) and 3D scattered intensity computations, but since this method computes the field at a certain distance  $z_n$  it is also applicable for computing the complex field. The beam is propagated for a fixed input field for a constant RI in every slice. Note that now the 2D method is derived. This method is again based on the inhomogeneous Helmholtz equation, but here it is rewritten in the matrix notation as follows

$$\frac{\partial \Phi}{\partial z} = \mathbf{H}(\mathbf{r}) \Phi(\mathbf{r}), \quad (2.23)$$

where

$$\Phi(\mathbf{r}) = \begin{pmatrix} U(\mathbf{r}) \\ \frac{\partial U(\mathbf{r})}{\partial z} \end{pmatrix}, \quad (2.24)$$

and

$$\mathbf{H}(\mathbf{r}) = \begin{pmatrix} 0 & 1 \\ -\frac{\partial^2}{\partial x^2} - k_m^2 (n_m^2 - n^2(\mathbf{r})) & 0 \end{pmatrix}. \quad (2.25)$$

The vector  $\Phi$  contains both the field and the  $z$ -derivative of the field. By splitting matrix  $\mathbf{H}(\mathbf{r})$  into a not spatially dependent scattering operator and a spatially dependent diffraction operator, we get  $\mathbf{H}(\mathbf{r}) = \mathbf{H}_1 + \mathbf{H}_2(\mathbf{r})$  with

$$\mathbf{H}_1 = \begin{pmatrix} 0 & 1 \\ -\frac{\partial^2}{\partial x^2} - k_m^2 n_m^2 & 0 \end{pmatrix}, \quad (2.26)$$

the propagation part and

$$\mathbf{H}_2(\mathbf{r}) = \begin{pmatrix} 0 & 0 \\ k_m^2(n_m^2 - n^2(\mathbf{r})) & 0 \end{pmatrix}, \quad (2.27)$$

the scattering part. By introducing these matrices, the matrix  $\mathbf{H}_1$  becomes spatial invariant describing the propagation in a homogeneous background medium. The system of Eq. 2.23 can be solved by approximating the equation as a first-order homogeneous linear system of differential equations. This solution then becomes

$$\Phi(z + \Delta z) = e^{\mathbf{H}_1 \Delta z} \Phi \approx \mathbf{P} \mathbf{Q}(z) \Phi(z), \quad (2.28)$$

with  $\Phi(z)$  the field and its  $z$ -derivative at slice  $z$ , and

$$\mathbf{P} = e^{\mathbf{H}_1 \Delta z}, \quad (2.29)$$

with  $\mathbf{P}$  describing the propagation of the wave and

$$\mathbf{Q}(z) = e^{\mathbf{H}_2(x,z) \Delta z}, \quad (2.30)$$

with  $\mathbf{Q}(z)$  describing the scattering of the wave. The propagation in the homogeneous background medium can be computed via  $\mathbf{P}$ , which can be solved using the Fourier transform [15]

$$\begin{aligned} \mathbf{P} \Phi &= \mathcal{F}_x^{-1} \{ \tilde{\mathbf{P}} \mathcal{F}_x \{ \Phi \} \}, \\ \mathbf{P} \Phi &= \mathcal{F}_x^{-1} \left\{ \begin{pmatrix} \cos k_z \Delta z & \frac{\sin k_z \Delta z}{k_z} \\ -k_z \sin k_z \Delta z & \cos k_z \Delta z \end{pmatrix} \mathcal{F}_x \{ \Phi \} \right\}, \end{aligned} \quad (2.31)$$

where  $\mathcal{F}_x$  and  $\mathcal{F}_x^{-1}$  represent the one-dimensional (1D) Fourier and inverse Fourier transform on the  $x$ -line. Furthermore,  $k_x$  is the corresponding  $\mathbf{k}$ -component which gives us  $k_z = \sqrt{k_m^2 n_m^2 - k_x^2}$  if  $k_x^2 \leq k_m^2 n_m^2$ , otherwise  $\tilde{\mathbf{P}} = \mathbf{0}$  in order to remove the evanescent component. The operator  $\mathbf{Q}(z)$  computes the scattered field induced by the difference in the refractive index at slice  $z$  and can be computed directly in real space by

$$\mathbf{Q}(z) \Phi = \begin{pmatrix} 1 & 0 \\ k_m^2(n_m^2 - n_x^2(z)) \Delta z & 1 \end{pmatrix} \Phi. \quad (2.32)$$

To find the solution of the wavefield at the position  $z_n$ , operators  $\mathbf{P}$  and  $\mathbf{Q}$  are recursively calculated slice-by-slice. As an initial condition for this algorithm, a plane wave is used at slice 0. Function  $\Phi$  for the plane wave is defined as

$$\Phi_0 = e^{ik_x^{in} x} \begin{pmatrix} 1 \\ ik_z^{in} \end{pmatrix}, \quad (2.33)$$

with  $k_x^{in} = 0$  and  $k_z^{in} = k_m$  for an incoming wave in the  $z$ -direction. The field at position  $z_n$  consists of both the forward and backward field. The backward field induces high-frequency artifacts [16], so we are only interested in the forward field. According to the principles of angular spectrum theory, any arbitrary field can be expressed as the sum of many plane wave components. By invoking linearity, the following relationship can be obtained [15]

$$\mathcal{F}_x \{ \Phi(z) \} = \begin{pmatrix} \mathcal{F}_x \{ U \} \\ \mathcal{F}_x \{ \frac{\partial U}{\partial z} \} \end{pmatrix} = \begin{pmatrix} 1 & 1 \\ ik_z & ik_z \end{pmatrix} \begin{pmatrix} \mathcal{F}_x \{ U_{\text{for}} \} \\ \mathcal{F}_x \{ U_{\text{back}} \} \end{pmatrix}, \quad (2.34)$$

with  $U_{\text{for}}$  and  $U_{\text{back}}$  the forward and backward field respectively. As a special case, any forward propagating illumination field  $U^{\text{in}}$  can be converted to

$$\Phi = \left( \mathcal{F}_x^{-1} \{ i k_z \mathcal{F}_x \{ U^{\text{in}} \} \} \right). \quad (2.35)$$

The transformation in Eq. 2.34 is invertible when the evanescent wave is not taken into consideration resulting in

$$\begin{pmatrix} \mathcal{F}_x \{ U_{\text{for}} \} \\ \mathcal{F}_x \{ U_{\text{back}} \} \end{pmatrix} = \frac{1}{2} \begin{pmatrix} 1 & \frac{-i}{k_z} \\ 1 & \frac{i}{k_z} \end{pmatrix} \begin{pmatrix} \mathcal{F}_x \{ U \} \\ \mathcal{F}_x \left\{ \frac{\partial U}{\partial z} \right\} \end{pmatrix} = \frac{1}{2} \begin{pmatrix} 1 & \frac{-i}{k_z} \\ 1 & \frac{i}{k_z} \end{pmatrix} \mathcal{F}_x \{ \Phi(z) \}. \quad (2.36)$$

The total forward field is then written as

$$U_{\text{for}} = \mathbf{F}\Phi = \mathcal{F}_x^{-1} \left\{ \left( \frac{1}{2}, \frac{-i}{2k_z} \right) \mathcal{F}_x \{ \Phi \} \right\}, \quad (2.37)$$

which can also be written as a series of matrices

$$U_{\text{for}} = \mathbf{F}\mathbf{P}\mathbf{Q}(z_{n-1}) \cdots \mathbf{P}\mathbf{Q}(z_1) \mathbf{P}\mathbf{Q}(z_0) \Phi_0. \quad (2.38)$$

## 2.2. The Inverse Problem

In order to reconstruct the refractive index from a set of measurements, three methods are used, of which two use the Fourier diffraction theorem. The other method is the inverse SSNP method.

### 2.2.1. The Fourier Diffraction Theorem

The Fourier diffraction theorem relates the diffraction pattern observed in the far-field region, for example, at a detector, to the spatial distribution of the object in the near-field region. The derivation is based on Mueller [10]. Instead of computing the refractive index  $n(\mathbf{r})$  directly, first, the scattering potential is computed, which is generally defined as

$$V(\mathbf{r}) = k_m^2 \left( 1 - \left( \frac{n(\mathbf{r})}{n_m} \right)^2 \right), \quad (2.39)$$

with  $n_m$  the refractive index of the surrounded medium. In the 2D case, the Green's function is proportional to the zero-order Hankel function of the first kind, as defined earlier in Eq. 2.13. This can be used together with the definition of this Hankel function to define the Green function [17]

$$H_0(k_m |\mathbf{r} - \mathbf{r}'|) = \frac{1}{\pi} \int dk_x \frac{e^{i[k_x(x-x') + \sqrt{k_m^2 - k_x^2}(z-z')]} }{\sqrt{k_m^2 - k_x^2}}, \quad (2.40)$$

$$G_{0+}(\mathbf{r} - \mathbf{r}') = -\frac{i}{4\pi} \int dk_x \frac{e^{i[k_x(x-x') + \sqrt{k_m^2 - k_x^2}(z-z')]} }{\sqrt{k_m^2 - k_x^2}}. \quad (2.41)$$

We define our incoming plane wave  $U_0(\mathbf{r})$  with amplitude  $a_0$ , propagation direction  $\mathbf{s}_0$  and wavenumber  $k_m$  as

$$U_0(\mathbf{r}) = a_0 e^{i k_m \mathbf{s}_0 \cdot \mathbf{r}}. \quad (2.42)$$

Using this as our definition, the first Born approximation in two dimensions reads

$$U_s^{(B)}(\mathbf{r}) = \iint d^2 r' G_{0+}(\mathbf{r} - \mathbf{r}') V(\mathbf{r}') U_0(\mathbf{r}') = \iint d^2 r' G_{0+}(\mathbf{r} - \mathbf{r}') V(\mathbf{r}') a_0 e^{i k_m \mathbf{s}_0 \cdot \mathbf{r}}. \quad (2.43)$$

Combining Eqs. 2.41 & 2.43 gives us

$$U_s^{(B)}(\mathbf{r}) = -\frac{i}{4\pi} \iint d^2 r' \int dk_x \frac{e^{i[k_x(x-x') + \sqrt{k_m^2 - k_x^2}(z-z')]} V(\mathbf{r}') a_0 e^{ik_m \mathbf{s}_0 \cdot \mathbf{r}}}{\sqrt{k_m^2 - k_x^2}}. \quad (2.44)$$

By introducing the Fourier transform of  $V(\mathbf{r}')$  as  $\mathcal{F}_x(V)(k_m(\mathbf{s} - \mathbf{s}_0))$  written as the integral over  $\mathbf{r}'$  as follows

$$\mathcal{F}_x(V)(k_m(\mathbf{s} - \mathbf{s}_0)) = \iint d^2 r' V(r') e^{-ik_m(\mathbf{s} - \mathbf{s}_0) \cdot \mathbf{r}'}, \quad (2.45)$$

and implementing this in the Born approximation such that

$$U_s^{(B)}(\mathbf{r}) = -\frac{ia_0}{4\pi} \int dk_x \frac{\mathcal{F}_x(V)(k_m(\mathbf{s} - \mathbf{s}_0)) e^{ik_m \mathbf{s} \cdot \mathbf{r}}}{\sqrt{k_m^2 - k_x^2}}. \quad (2.46)$$

This equation is true for every angle  $\phi$  where the detector is placed and the position vector  $\mathbf{r} = (x_D, l_0)$ , with  $x_D$  the position on the detector and  $l_0$  the distance from the center of the object to the detector. To arrive at the Fourier Diffraction Theorem, one will perform a 1D Fourier transform of  $U_B(\mathbf{r})$  along  $x_D$  such that

$$\mathcal{F}_{x_D}(U_s^{(B)})(k_{Dx}, \phi) = -\frac{ia_0}{4\pi} \int dx_D \int dk_x \frac{\mathcal{F}_x(V)(k_m(\mathbf{s} - \mathbf{s}_0))}{\sqrt{k_m^2 - k_x^2}} e^{ik_x x_D + i\sqrt{k_m^2 - k_x^2} l_0} e^{-ik_{Dx} x_{Dx}}. \quad (2.47)$$

By identifying the delta distribution as

$$\delta(k_x - k_{Dx}) = \frac{1}{2\pi} \int dx_D e^{i(k_x - k_{Dx}) x_D}, \quad (2.48)$$

and implementing this in Eq. 2.47, by replacing all  $k_x$  with  $k_{Dx}$  and applying the prefactor, the equation will reduce to

$$\mathcal{F}_{x_D}(U_s^{(B)})(k_{Dx}, \phi) = -\frac{ia_0}{2} \frac{\mathcal{F}_x(V)(k_m(\mathbf{s} - \mathbf{s}_0))}{\sqrt{k_m^2 - k_{Dx}^2}} e^{i\sqrt{k_m^2 - k_{Dx}^2} l_0}. \quad (2.49)$$

Via this equation, one can find the Fourier Transform of the scattering potential as follows

$$\mathcal{F}_x(V)(k_m(\mathbf{s} - \mathbf{s}_0)) = -\frac{2}{ia_0} \sqrt{k_m^2 - k_{Dx}^2} \mathcal{F}_{x_D}(U_s^{(B)})(k_{Dx}, \phi) e^{-i\sqrt{k_m^2 - k_{Dx}^2} l_0}. \quad (2.50)$$

In order to eliminate  $a_0$  in this equation, one uses the following trick

$$\frac{\mathcal{F}_x\{U_s^{(B)}(x)\}}{a_0} = \mathcal{F}_x\left\{\frac{U_s^{(B)}(x)}{U_0(l_0)} e^{ik_m l_0}\right\} = \frac{\mathcal{F}_x\{U_s^{(B)}\} e^{ik_m l_0}}{U_0(l_0)}. \quad (2.51)$$

Using this substitution gives us the Fourier Diffraction Theorem

$$\mathcal{F}_x(V)(k_m(\mathbf{s} - \mathbf{s}_0)) = -\frac{2}{i} \sqrt{k_m^2 - k_{Dx}^2} e^{-i(\sqrt{k_m^2 - k_{Dx}^2} - k_m) l_0} \mathcal{F}_{x_D}(U_s^{(B)})(k_{Dx}, \phi). \quad (2.52)$$

Since we are only interested in propagating waves, we reconstruct the scattering potential with disregarding the evanescent waves by applying a filter such that only the values  $k_{Dx}^2 < k_m^2$  are accounted for, otherwise  $\mathcal{F}_x(V)(k_m(\mathbf{s} - \mathbf{s}_0)) = 0$ . The Fourier transform of the scattered wave  $\mathcal{F}_{x_D}(U_s^{(B)})(k_{Dx}, \phi)$  needs to be placed on semi-circular arcs in Fourier space such that

$$k_m(\mathbf{s} - \mathbf{s}_0) = \left(k_{Dx} \cos \phi - \sqrt{k_m^2 - k_{Dx}^2} \sin \phi, k_{Dx} \sin \phi + \sqrt{k_m^2 - k_{Dx}^2} \cos \phi\right). \quad (2.53)$$

This results in rotated circular arcs in the Fourier space, as shown in Fig. 2.1. This is the case for the sample rotation (OR) method, in which the entire object gets rotated at a fixed angle of incidence. By doing this, the Ewald sphere (red-dotted line) gets fully captured. By increasing the number of projections  $N_\phi$ , the Ewald sphere gets more and more filled. By interpolating the sampled data onto a Cartesian frequency grid, as in the right figure, a 2D inverse Fourier transform can be computed in order to find the scattering amplitude, which can be easily converted into the refractive index by solving Eq. 2.39.

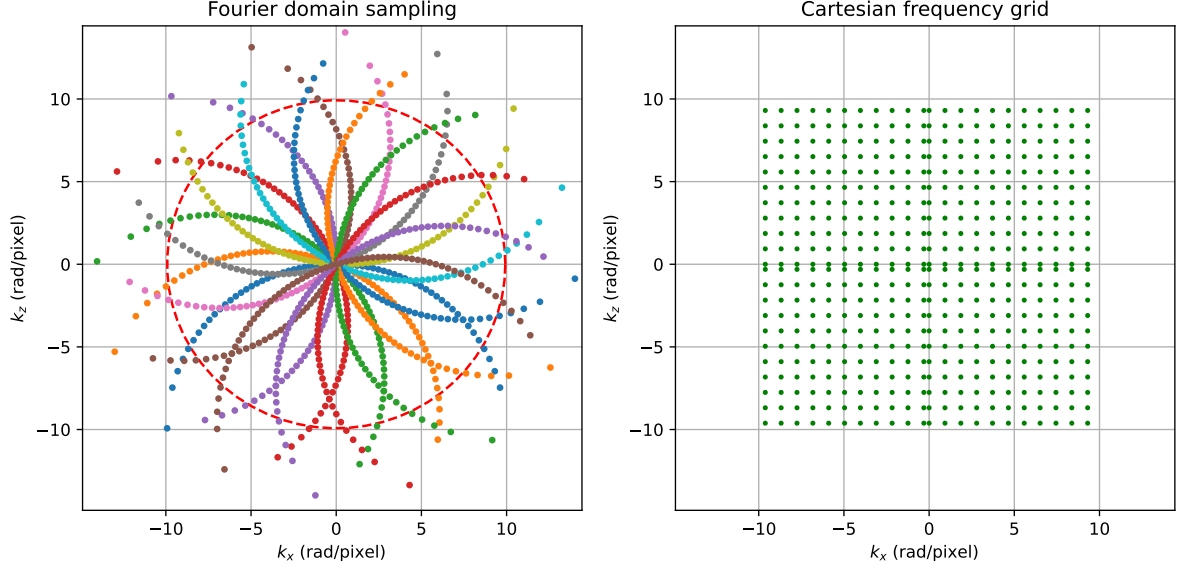


Figure 2.1: The Fourier sampling for the OR method. The arcs get rotated over the angle  $\phi$ , which results in full coverage of the Ewald sphere (red-dotted line). By interpolating the rotated arcs on a rectangular Cartesian frequency grid, as shown in the right figure, a 2D inverse Fourier transform can give the scattering amplitude  $V(\mathbf{r})$ .

The reconstruction with the illumination scanning (LA) method is comparable to the OR method. However, now the illumination angles are varied at a fixed detection angle which results in a different position of the circular arcs in the Fourier space such that

$$k_m(\mathbf{s} - \mathbf{s}_0) = \left( k_{Dx} - k_m \sin \phi, \sqrt{k_m^2 - k_{Dx}^2} + k_m(1 - \cos \phi) \right), \quad (2.54)$$

where the angles are illustrated in Fig. 2.2. This figure also shows the data used by the dotted black lines.



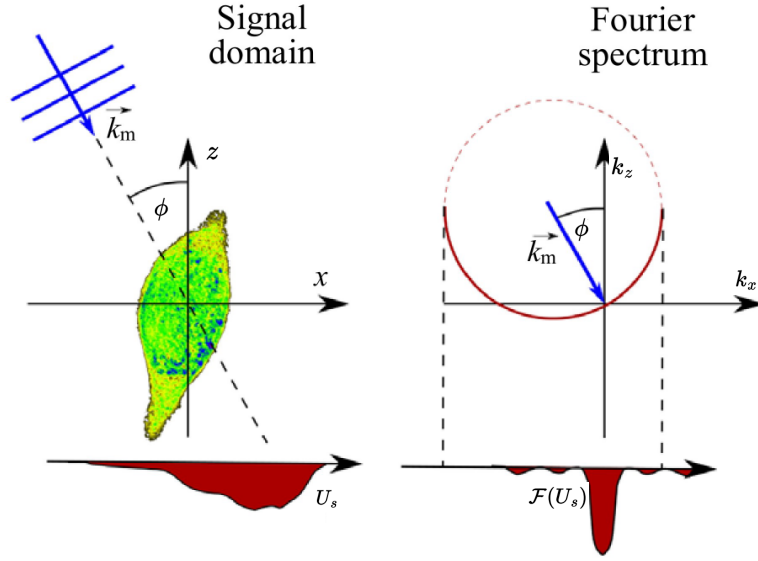


Figure 2.2: The LA method in the real and Fourier space. A plane wave comes in at angle  $\phi$  and the red Ewald sphere gets a shift. This figure is modified from Kuś [4].

This shift makes  $k_x$  potentially twice as wide, and therefore, the data can be interpolated on a potentially twice as big grid, because more information is now visible in the Fourier space. This can lead to a resolution improvement in the lateral direction of a factor of 2. Figure 2.3 shows the shifted arcs together with the original Ewald sphere (red-dotted line) from the OR method and the limiting Ewald sphere (black-dotted line). The potential of a twice as big interpolation grid compared to the OR method is shown by the red rectangle, which is the interpolation grid of the OR method. The blue areas show the missing cone artifact, which is a potential downside of the LA method. Due to the way, the arcs get shifted, there is a part in the original Ewald sphere that does not have sampling points, so there is no information about the object in those areas. By interpolating the data on the Cartesian frequency grid, the scattering potential can be obtained by computing the 2D inverse Fourier transform.

The limitation of the FDT method is that it is based on the Born approximation, which only accounts for single scattering. Therefore, this method is only valid for reconstructing the RI of low contrast scatterers. The SSNP model does not make the single scattering assumption and, therefore, has the potential to reconstruct the RI of multiple scatterers.

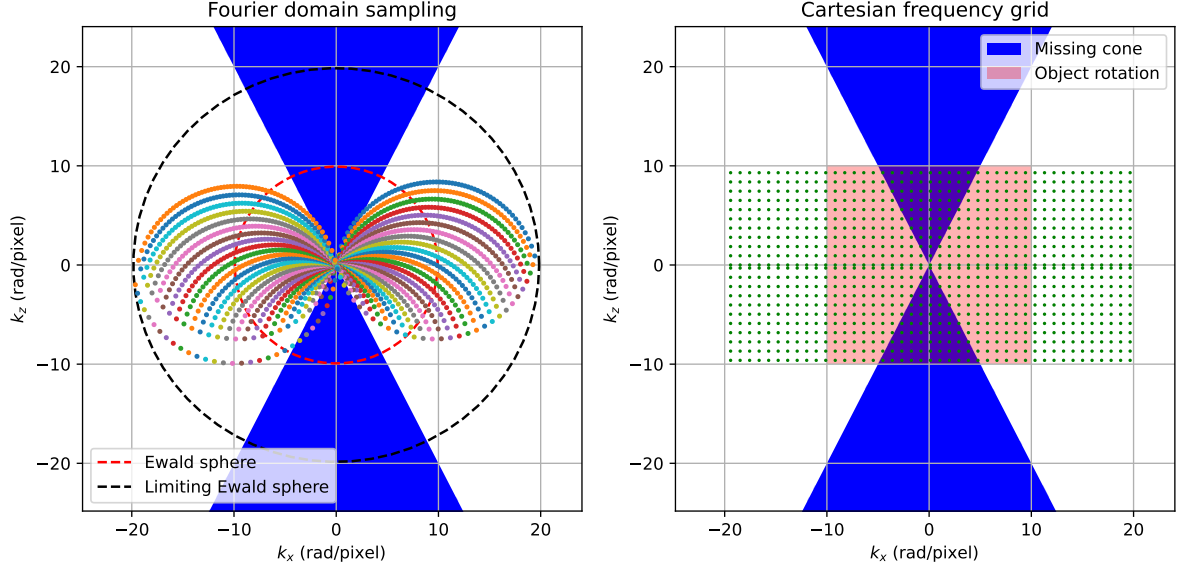


Figure 2.3: The Fourier domain sampling for the LA method. The arcs get shifted over the incoming angle. The sampling is twice as wide as in the sample rotation method, leading to a twice as wide Cartesian frequency grid for the reconstruction. The sampling leaves a missing triangle (blue area), better known as the missing cone artifact.

### 2.2.2. SSNP-based Tomographic Reconstruction

To reconstruct the refractive index from the measured data with the SSNP model, an optimization problem is introduced as

$$\hat{n} = \operatorname{argmin}_n \left\{ \left\| U_s^{\text{for}} - U_s^{\text{meas}} \right\|_2^2 + \left\| \sqrt{I_s^{\text{for}}} - \sqrt{I_s^{\text{meas}}} \right\|_2^2 + \tau R_{\text{TV}}(n) \right\}, \quad (2.55)$$

with  $\hat{n}$  the estimated of the refractive index for which the function inside the argmin is minimal, and  $I_s^{\text{for}}$  and  $I_s^{\text{meas}}$  the obtained intensity from the scattered field of respectively the SSNP forward model and the measured data. Two  $L_2$ -norms are taken, to consider both phase and intensity differences. The intensity does not have to be there explicitly since this is already accounted for in the first term. However, the SSNP model is generally more accurate for the intensity computation than for the phase computation [15]. By including an extra intensity norm, the optimization equation accounts more value for the intensity than the phase. The last term is a regularization term which is included to prevent overfitting [18]. In this thesis, the  $L_1$ -norm of the refractive index is chosen, however, there are other possibilities, such as the derivative of the refractive index as the input for the  $L_1$ -norm [19]. Because this will enlarge the computational complexity of an already highly complex problem, this regularization is not taken due to the addition of the computation of a second-order derivative. The variable  $\tau$  is the regularization parameter which is set equal to 0.2 in line with the work of Zhu et al. [11].

The optimization problem is shown in Fig. 2.4. Via the estimate of the RI, a field is computed at the detector using the SSNP forward model. By optimizing Eq. 2.55, a new estimation of the RI is computed, which is then used to compute a new field at the detector until the stopping criteria are reached. The initialization of the refractive index is either the background RI  $n_m$  or the RI computed using the Fourier diffraction theorem based on the Born approximation.

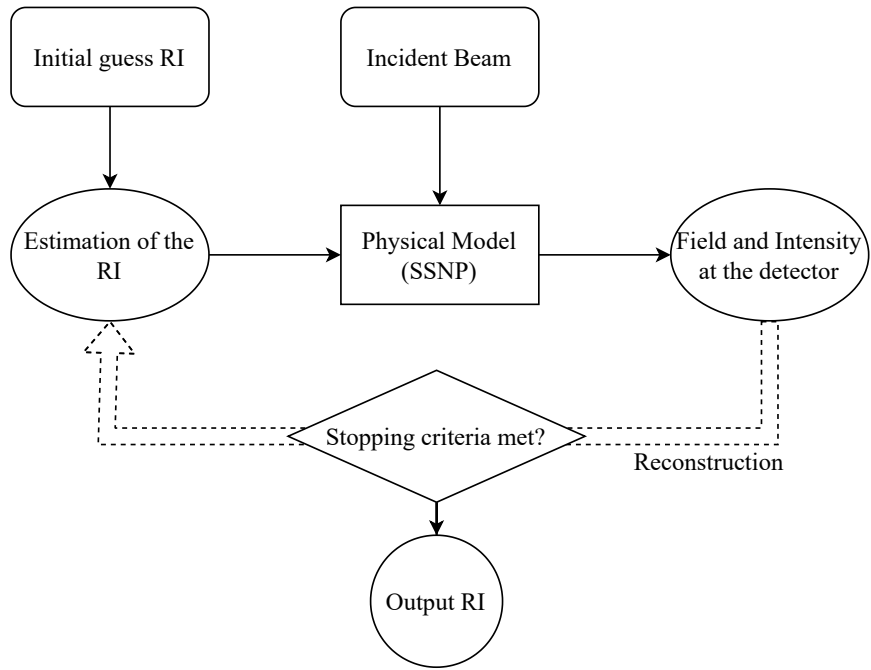


Figure 2.4: The optimization problem of the SSNP model, where the RI is computed iteratively by optimizing Eq. 2.55.

# 3

## Methods

The theory discussed in the previous chapter is implemented in Python 3.9.13 [20] to perform quantitative analysis. The computations are done on a computer with the Intel Core i7-9750H Processor [21] from 2019. This chapter describes the essential parts of the code, the most important used packages, and how code performances are analyzed. A commented implementation of all the theory can be found on Github<sup>1</sup>.

### 3.1. Implementation

The forward Mie scattering model is implemented using simple for-loops. The Bessel and Hankel functions are used from the *scipy.special*-package (*jv* and *hankel1*) [22].

For the forward SSNP model, a sequential model is used. To avoid unnecessary extra memory and memory collection time, only the last value of the field at each iteration is saved. The Fourier transform in this computation is performed with the *Numpy*-package [23] with the fast Fourier transform (FFT). The FFT reduces the complexity to  $\mathcal{O}(N_x \log N_x)$  for  $N_x = N^2$ , with  $N$  an integer and  $N_x$  the number of points at the detector, instead of  $\mathcal{O}(N_x^2)$  for all other  $N_x$  [24]. Therefore, only  $N_x = N^2$  number of points are used in the implementation. The sequential model is performed by one big for loop, which computes  $\Phi$  at every slice.

Refractive index reconstruction is the most computationally complex and time-consuming part. For the reconstruction using FDT, an interpolation is performed to find the data on the Cartesian frequency grid such that the 2D spatial frequency inverse Fourier transform can be computed. This interpolation is done by the *scipy.interpolate*-package [22]. The function *scipy.interpolate.griddata* uses Delaunay triangulation to determine the local neighborhood of each grid point and linear Barycentric interpolation to determine the values on the given new grid. The Delaunay triangulation scales with  $\mathcal{O}(N \log N)$  with  $N$  the amount of given grid points [25]. Therefore, if  $N_x$  or  $N_\phi$  increases, the computation time also increases. The linear Barycentric interpolation scales with  $\mathcal{O}(M)$  with  $M$  the number of interpolation points [26]. This method uses the three closest points to compute the value at the desired location. The three points get a certain weight depending on the distance to the grid points. When the interpolated grid is computed, the *numpy.fft.iff2*-function performs a 2D inverse FFT.

For the reconstruction using the SSNP model, the *TensorFlow*-package [27] is used, which uses automatic differentiation to compute the derivative of the forward SSNP model. This is needed to update

---

<sup>1</sup><https://github.com/brijn02/ODT.git>

the refractive index iteratively. Automatic differentiation uses the exact derivative of certain functions, and by implementing the chain rule, it can compute the derivative of complex functions [28]. With the derivative of the SSNP model towards the RI, the estimate of RI can be updated following the stochastic gradient descent (SGD) method, which needs a specific learning rate  $\alpha$  to compute the updated value:

$$n_{i+1} = n_i - \alpha \frac{\delta \hat{n}}{\delta n_i}, \quad (3.1)$$

with  $n_i$  the estimate of the refractive index at iteration  $i$  and  $\hat{n}$  the optimization equation (Eq. 2.55). The iterative scheme is shown in Fig. 3.1. With the initial guess, the complex field at the detector is computed together with its gradient. It is checked if the maximum number of iterations is reached or the loss increases. The loss is defined as

$$\text{loss} = \left\| U_s^{\text{for}} - U_s^{\text{meas}} \right\|_2^2 + \left\| \sqrt{I_s^{\text{for}}} - \sqrt{I_s^{\text{meas}}} \right\|_2^2 + \tau R_{\text{TV}}(n). \quad (3.2)$$

The last check is for stability reasons. The loss tends to explode if this *if*-statement is not included. If one of the two tests is true, the model will check whether the maximum number of angular projections is reached. If not, the angle will be updated. The RI gets rotated with the *scipy.ndimage.rotate*-function [22] over the angle step  $\frac{360}{N_\phi}$  and a new computation for the next angle begins. When all tests are true, the reconstruction is finished with a new refractive index.

The *Param*-package [29] is used for code simplicity. This package consists of a Python class that automatically updates specific values when a parameter changes. For example, the wavelength  $\lambda_0$  gets changed, and, therefore, the value of the wavenumber  $k_m$  gets automatically updated. Another benefit of this package is that only one class is needed for passing values into a function instead of passing all the values one by one.

### 3.2. Data Analysis

For the analysis of the data, multiple techniques are used. For comparing the forward field, the root mean square error (RMSE) is used, which is defined as

$$\text{RMSE} = \sqrt{\frac{\sum_{i=0}^N \|\hat{y}_i - y_i\|^2}{N}}, \quad (3.3)$$

with  $\hat{y}_i$  the exact solution and  $y_i$  the measured solution at position  $i$ . The benefit of this error is that outliers get penalized more than the mean absolute error (MAE) [30].

For the data analysis of the refractive index, the structural similarity index (SSIM) is used. This measure was introduced by Wang et al. [31] and considers three measures: luminance, contrast, and structural comparison. The luminance comparison is obtained using the mean in the refractive index's  $x$ - and  $z$ -axis. The contrast comparison is defined by the standard deviation, and the structural comparison is defined by the refractive index minus the mean and divided by the standard deviation as follows

$$s(\mathbf{x}, \mathbf{z}) = f\left(\frac{\mathbf{x} - \mu_x}{\sigma_x}, \frac{\mathbf{z} - \mu_z}{\sigma_z}\right), \quad (3.4)$$

with  $s(\mathbf{x}, \mathbf{z})$  the structural comparison,  $\mu_i$  the mean in the  $i$ -direction,  $\sigma_i$  the standard deviation in the  $i$ -direction and  $f(\cdot, \cdot)$  the function between both. This is implemented in the *scikit-image*-package in Python [32], which is used to compute the SSIM for the results.

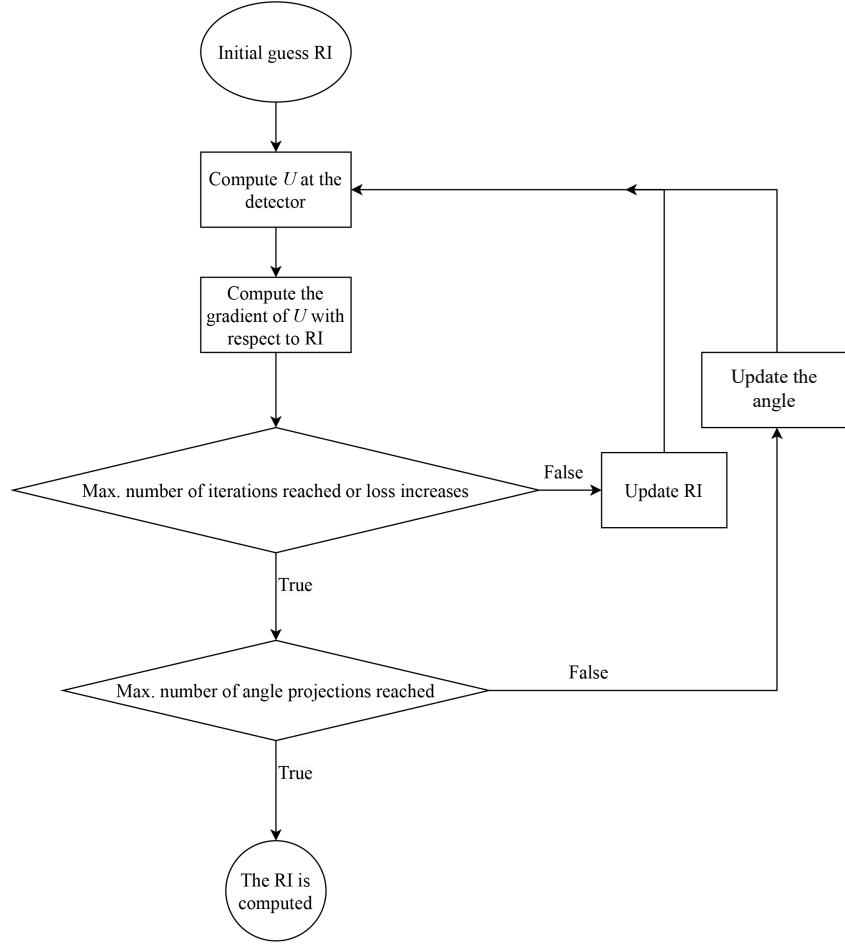


Figure 3.1: The flowchart of the reconstructed model.

To compute the point-by-point difference between two refractive indices, the percentage error  $E$  is used, which is defined as

$$E = \frac{\hat{y} - y}{\hat{y}} \cdot 100\%, \quad (3.5)$$

with  $\hat{y}$  the exact solution and  $y$  the measured solution. The results are in percentage as a measure of difference.

In this thesis, the computation time is the wall clock computation time, which is all the time that passes from the start of a task until the end. This is measured by the built-in Python *time*-module. To calculate the speed up, the following equation is used

$$\text{Speed up} = \frac{t(\text{Original program})}{t(\text{New program})}, \quad (3.6)$$

with  $t$  the time of one measurement.

# 4

## Results

This chapter presents the results of the different numerical implementations of the earlier discussed theory. The results are divided into a forward and an inverse problem. The different implementations are compared, and their computation time and reconstruction accuracy are shown.

### 4.1. The Forward Scattering Problem

In the forward problem, the exact field is first compared with the Born and Rytov approximation, and after that, the exact field is compared to the solution obtained with the SSNP model. The scattered field is computed for a cylinder with homogeneous RI  $n_{\text{cyl}}$  in a homogeneous background RI  $n_m$ .

#### 4.1.1. The Exact Field against the Born Approximation

The magnitude of the scattered field is shown in Fig. 4.1 for different  $n_{\text{cyl}}$ . The exact field and both the Born and Rytov approximation are plotted. The refractive index differs from  $n_{\text{cyl}} = 1.01$  (top-left) to  $n_{\text{cyl}} = 1.07$  (bottom-right) in steps of  $\delta n_{\text{cyl}} = 0.02$ . The wavelength  $\lambda_0 = 0.633$  mm, the background RI  $n_m = 1.0$ , the radius  $R_0 = 4\lambda_0$ , the incoming angle  $\phi_0 = 0.0$  and half the width of the detector  $x_0 = 16\lambda_0$  are the same for most simulations presented in this chapter unless otherwise stated. Furthermore, in this simulation  $N_x = 1024$  and the distance to the detector  $l_0 = 4\lambda_0$ . For an increasing  $n_{\text{cyl}}$ , the Born approximation differs more from the exact field. The Rytov approximation also differs more for increasing  $n_{\text{cyl}}$ . However, the difference between the exact field and the Rytov approximation is far smaller than the difference between the exact field and the Born approximation.

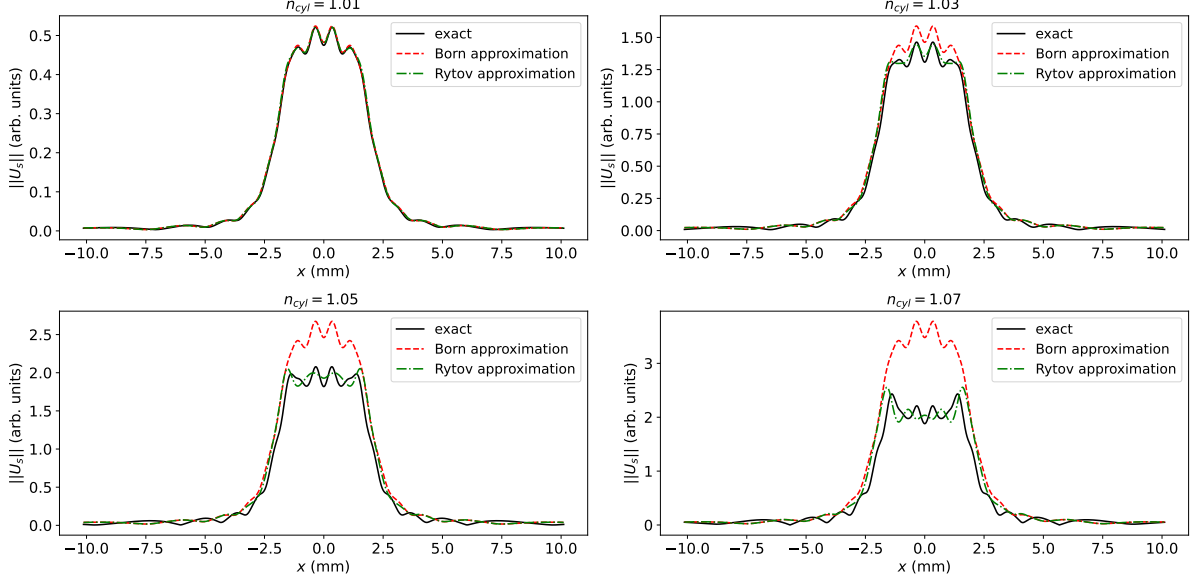


Figure 4.1: The magnitude of the scattered field measured at the detector with width  $2x_0 = 32\lambda_0$  computed for different  $n_{\text{cyl}}$  varying from  $n_{\text{cyl}} = 1.01$  (top-left) to  $n_{\text{cyl}} = 1.07$  (bottom-right) in steps of  $\delta n_{\text{cyl}} = 0.02$ . The exact field and both the Born- and Rytov-approximation are shown.

The unwrapped phase of the exact field and the Born and Rytov approximation is shown in Fig. 4.2. The figure shows the same situation as in Fig. 4.1, but now the phase is plotted. Different from the magnitude, the Born and Rytov approximations are closer to each other and differ more from the exact field for increasing  $n_{\text{cyl}}$ .

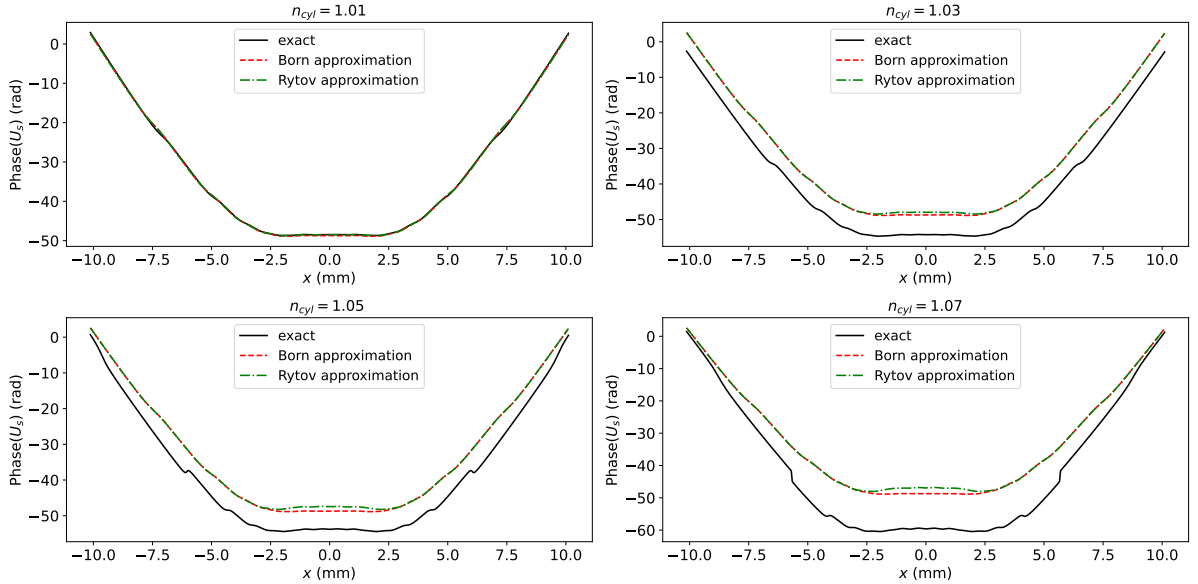


Figure 4.2: The phase of the scattered field measured at the detector with width  $2x_0 = 32\lambda_0$  computed for different  $n_{\text{cyl}}$  varying from  $n_{\text{cyl}} = 1.01$  (top-left) to  $n_{\text{cyl}} = 1.07$  (bottom-right) in steps of  $\delta n_{\text{cyl}} = 0.02$ . The exact field and both the Born- and Rytov-approximation are shown.



The RMSE of the exact field compared with the Born and Rytov approximations are shown for increasing  $n_{\text{cyl}}$  with the same parameters as discussed above in Fig. 4.3 with a log-scale on the RMSE-axis. In accordance with Figs. 4.1-4.2, the error increases for increasing  $n_{\text{cyl}}$ . The error of the Rytov approximation has the same pattern as the Born approximation. However, the error is structurally lower than the Born approximation. This is because the Rytov approximation is generally more accurate than the Born approximation.

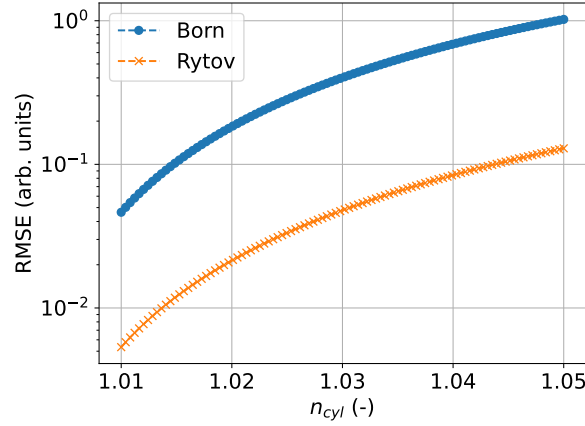


Figure 4.3: The RMSE of the exact field compared with the Born and Rytov approximation for increasing  $n_{\text{cyl}}$  plotted with a log-scale on the RMSE-axis.

#### 4.1.2. The Forward SSNP Method

For the forward SSNP method, the magnitude (left) and phase (right) of the scattered field of a cylinder with  $n_{\text{cyl}} = 1.01$  is shown in Fig. 4.4 together with the exact field. The distance to the detector is  $l_0 = 16\lambda_0$  and the total propagating distance  $z_n = 2l_0$ . The number of points in the  $x$ - and  $z$ -direction are set equal such that  $N_x = N_z = 2048$ . Both the phase and magnitude show convergence to the exact solution, but the SSNP model shows some ripples around the solution, especially in the outer parts close to the edge of the detector. The phase also shows some offset at the outer parts of the detector, which is related to the ripples in the magnitude plot. These ripples could originate from aliasing.

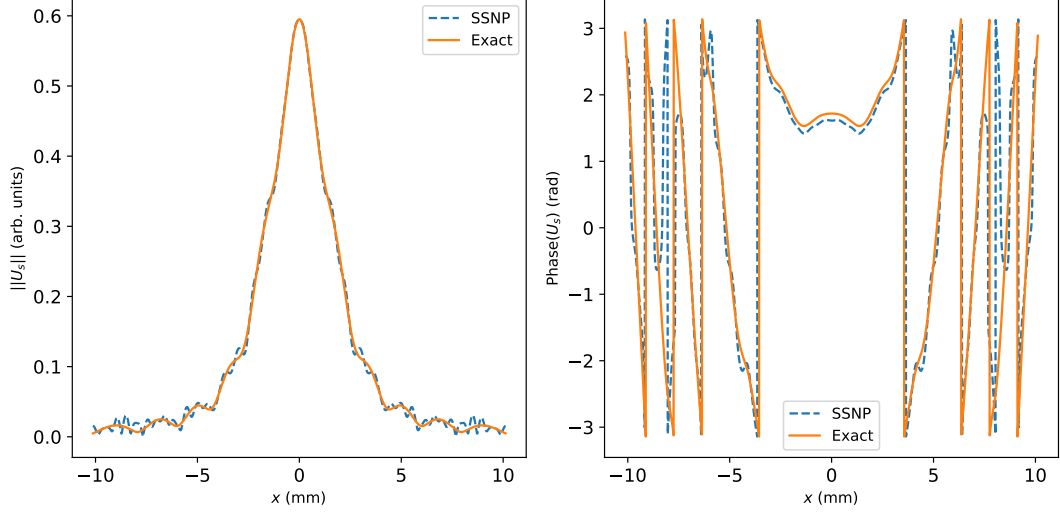


Figure 4.4: The magnitude (left) and the phase (right) of the scattered field obtained with the exact data and the SSNP forward model for a Cylinder with radius  $R_0$  and refractive index  $n_{\text{cyl}} = 1.01$ .

Figure 4.5 shows a study of the error as a function of the cylinder's step size, lateral step size, and refractive index. The left figure shows that the RMSE decreases for a decreasing step size  $\Delta z = \frac{z_n}{N_z}$  with a constant  $N_x = 2048$  and a log scale at both axes. Until  $\Delta z = 10^{-2}$ , the error decreases linear. This is in accordance with what was reported in the literature [11]. After that, the convergence slowly stops for decreasing  $\Delta z$ . The middle figure shows the RMSE for increasing  $\Delta x$  with a constant  $N_z = 2048$  and a log scale at both axes. The same linear convergence rate is visible as for  $\Delta z$ . There is also a stop in the convergence rate. The error could be slightly off compared to the literature due to the floating point precision of the field. The right figure shows the convergence for increasing  $n_{\text{cyl}}$ . The error increases linearly for an increasing  $n_{\text{cyl}}$ . This error is obtained with  $N_z = N_x = 4096$ .

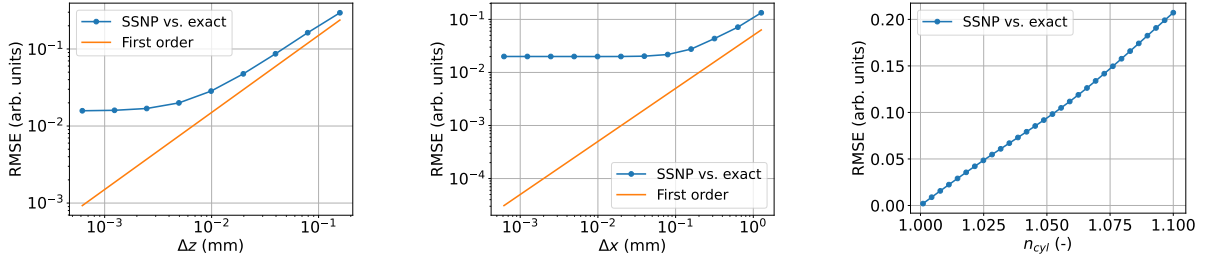


Figure 4.5: The convergence plots for  $\Delta z$  (left),  $\Delta x$  (middle) and  $n_{\text{cyl}}$  (right) which show the RMSE for different values obtained with the SSNP model.

## 4.2. The Inverse Problem

For the results of the inverse problem, first, the FDT is shown with the Born field as input data, together with code performance plots such as the computation time and reconstruction accuracy for both sample rotation (OR) and illumination scanning (LA). After that, the SSNP model results are discussed with the FDT obtained with analytical field data. Only the sample rotation is used for this. Furthermore, the code performance of the SSNP model is discussed. In this section, only the real parts of the reconstructions are used. However, the FDT allows the reconstruction of complex scatterers. As a proof of concept, a complex reconstructed refractive index is shown in Fig. A.1 in the Appendix. Again all the computations are performed on a cylinder with a homogeneous RI  $n_{\text{cyl}}$  in a

homogeneous background RI  $n_m$ .

#### 4.2.1. Fourier Refractive Index Reconstruction under the Born Approximation

The tomographic refractive index reconstruction obtained with the FDT using the Born field as input data is shown in Fig. 4.6 for both the OR and LA method. This figure also indicates the cross-sections for Fig. 4.7. The reconstruction is obtained with the Born field, so only single scattering is included. Because the LA method works better (more accurately) for a wider detector, such that more information about the field can be obtained, the detector width is twice the standard such that  $x_0 = 32\lambda_0$ . For the LA method, the maximum input angle is set to  $\phi_{\max} = 0.45\pi$ . The minimum value is then  $\phi_{\min} = -0.45\pi$ . The number of points is  $N_x = 2048$ , and the number of angular projections is  $N_\phi = 64$ . Sinograms of both methods and their Fourier transform can be found in the Appendix in Figs. A.2-A.3. The reconstructed RI is circular symmetric for the OR method, which is expected since every input angle has the same field. The LA method shows a good reconstruction in the  $x$ -direction, however, in the  $z$ -direction, there are some offsets because of the missing cone artifact.

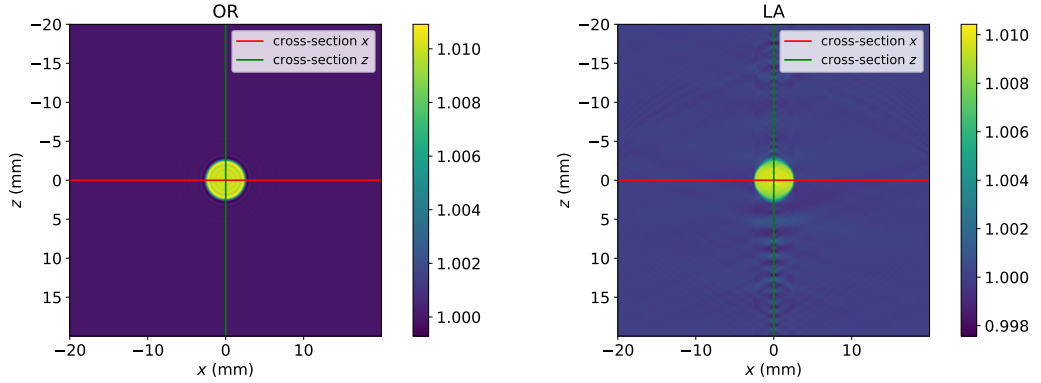


Figure 4.6: The 2D refractive index obtained with the Born field as input for  $N_x = 2048$  and  $N_\phi = 64$ . The lines represent the cross-sections for Fig. 4.7. The left figure shows the reconstructed RI with the OR method, and the right figure shows the reconstructed RI with the LA method.

The intersections of the tomographic refractive index reconstruction in the  $x$ - and  $z$ -direction of both the OR and LA method are shown in Fig. 4.7 together with the exact object for  $n_{\text{cyl}} = 1.01$ . This figure corresponds to the same RI as in Fig. 4.6. In the  $x$ -direction, both methods converge to the exact solution with some fluctuations around the exact RI. In the  $z$ -direction, the middle of the reconstructed RI of the cylinder has some offsets from the ground truth solution with the LA method, which is in accordance with the missing cone artifact. Since the OR method is circularly symmetric, the same result is obtained in both directions.

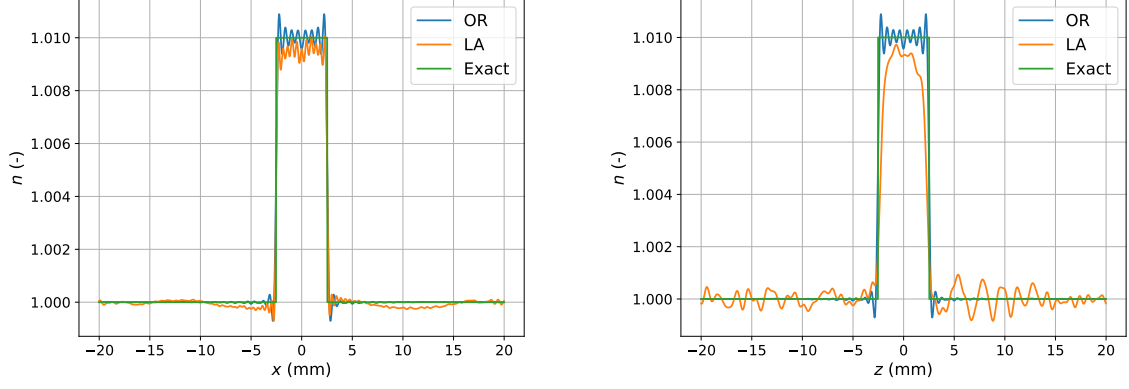


Figure 4.7: The reconstruction of the refractive index with the Born approximated field for  $N_x = 2048$  and  $N_\phi = 64$ . The intersections in the middle of the cylinder are shown in both the  $x$ - (left) and  $z$ -direction (right).

To compute the error of the tomographic refractive index reconstruction obtained with the Born approximation, the SSIM is used. Figure 4.8 shows this SSIM for both an increase in the number of points on the detector  $N_x$  (left) as well as angular projections  $N_\phi$  (right) for both methods with a log-scale for  $N_x$  as well as  $N_\phi$ . For the plot with varying  $N_x$ ,  $N_\phi = 64$  and  $x_0 = 32\lambda_0$  for the same reason as mentioned earlier. The figure shows that for a low amount of sample point  $N_x \leq 32$ , the SSIM is higher for the LA method. For  $N_x > 32$ , the SSIM is higher for the OR method. The SSIM converges to 1 for increasing  $N_x$  for both methods. In the right figure, the varying angular projections  $N_\phi$  are shown with  $N_x = 512$ . There is an increase in SSIM visible for both methods until  $N_\phi = 64$ . After that, the SSIM stays about constant for both methods. Unlike the increase in  $N_x$ , the increase in  $N_\phi$  does not lead to a SSIM of 1, which indicates that  $N_x$  is the dominating factor for the computation of the error.

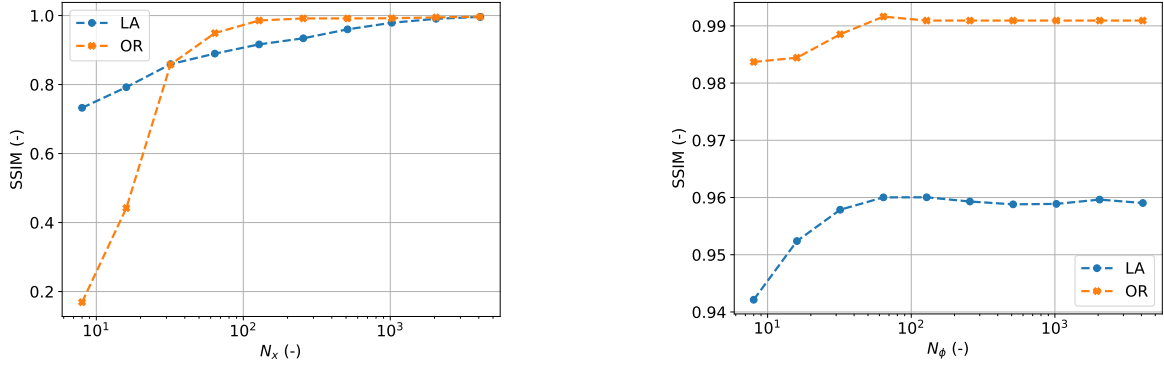


Figure 4.8: The structural similarity index (SSIM) for increasing  $N_x$  (left) and  $N_\phi$  (right) with a log-scale on the  $N_{x,\phi}$ -axis.

The computation time of both methods, divided into the most computation time-consuming functions, is shown in Fig. 4.9 for increasing  $N_x$  and in Fig. 4.10 for increasing  $N_\phi$ . For Fig. 4.9, the number of projections  $N_\phi = 64$  and for Fig. 4.10  $N_x = 64$ . The left and middle figures show the most time-consuming function in both methods and the total computation time for both the OR method (left) and the LA method (middle). The *scipy.intp.griddata*-function takes the most computation time in both methods due to the Delaunay triangulation and the Barycentric interpolation. The second most time-consuming part is the *np.fft.iff2*-function which is the inverse fast Fourier transform in 2D. The 1D FFT costs virtually no computation time compared to the *scipy.intp.griddata*- and the

*np.fft.ifft2*-function. The right figure shows the total computation time of both methods together with a linear ( $N$ ) and a quadratic power law line ( $N^2$ ) for visualization purposes only. For low  $N_x$ , both are close to each other, but for  $N_x \geq 1024$ , the LA method takes about twice as much time. For both methods, the first part is of order  $\mathcal{O}(N_x)$  and towards  $N_x \geq 1024$  the order is  $\mathcal{O}(N_x^2)$ .

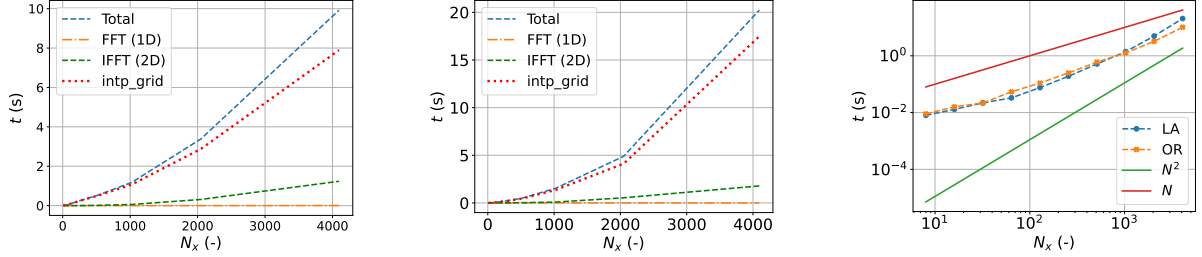


Figure 4.9: The computation time of both methods for increasing  $N_x$  divided into the most computation time-consuming parts of the computation for the OR (left) and LA (middle) method and the total computation time of both methods on a log-log plot (right).

For increasing  $N_\phi$ , the most computation time consuming part is still the *scipy.intp.griddata*-function. The execution of this function uses almost completely all the computation time. The LA method is faster than the OR method for every  $N_\phi$ . This could be because the grid is wider in the LA method, making it easier to perform Delaunay triangulation. For increasing  $N_x$ , eventually, this benefit disappears since the LA is slower for  $N_x \geq 1024$ , which could be due to the bigger interpolation grid.

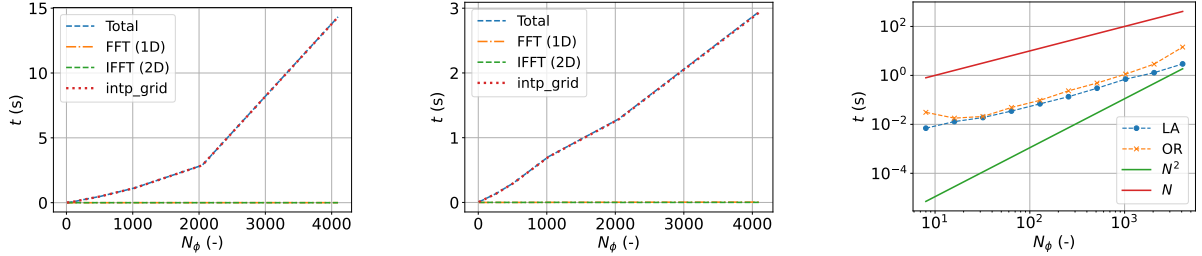


Figure 4.10: The computation time of both functions for increasing  $N_\phi$  divided into the most computation time-consuming parts of the computation for the OR (left) and LA (middle) method and both on a log-log plot (right).

#### 4.2.2. Iterative Reconstruction with the SSNP Model

Now we compare the FDT reconstruction with the SSNP-based iterative reconstruction. In contradiction to the previous section, the exact field is now used as an input field instead of the Born field. Note that the comparison is based on the sample rotation case. The comparison is shown in Fig. 4.11, where the results of the different methods are plotted for different  $n_{\text{cyl}}$ . The ground truth object is a cylinder with a homogeneous refractive index with  $n_{\text{cyl}}$  and a background medium  $n_m = 1.0$ . The results are obtained with  $N_\phi = 64$  for all simulations. The number of points is equal in the  $x$ - and  $z$ -direction such that  $N_x = N_z = 2048$ . The reconstruction of the refractive index using the FDT still accurately represents the RI for  $n_{\text{cyl}} = 1.001$  and  $n_{\text{cyl}} = 1.01$  despite using exact field data. Figures 4.1-4.2 showed that there is a difference between the exact field and the Born approximation for  $n_{\text{cyl}} = 1.05$  which can also be seen in the tomographic reconstruction. The reconstruction for  $n_{\text{cyl}} = 1.05$  does not come close to the ground truth solution because the multiple scattering is not

considered in the FDT method. For the SSNP model, the reconstruction works for all the  $n_{\text{cyl}}$  since it does not assume single scattering. The reconstruction of the SSNP model now uses the background refractive index as input for the total field. The learning rate is  $\alpha = 2, 20, 50$  respectively, and the max. number of iterations is 20 for all  $n_{\text{cyl}}$ . The relative error  $E$  of all the figures is shown in the Appendix in Fig. A.4.

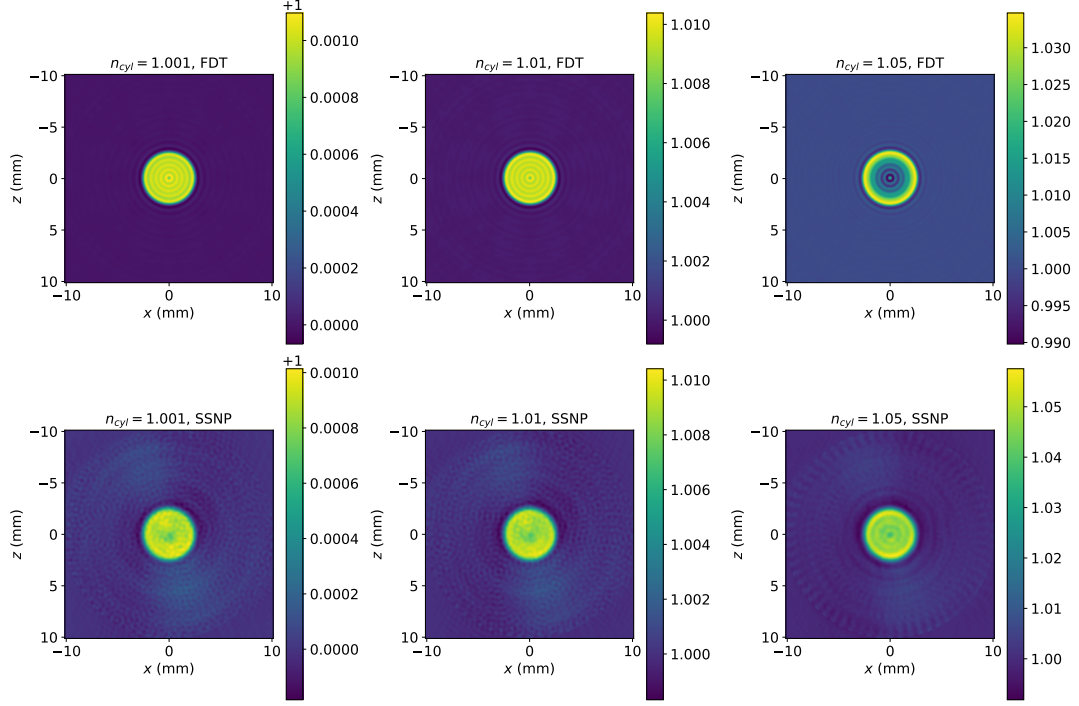


Figure 4.11: The reconstruction of a cylinder with refractive index  $n_{\text{cyl}} = 1.001, 1.01, 1.05$  with the FDT, and SSNP method. The reconstruction is computed with exact field data.

The intersection in the middle of the cylinders of Fig. 4.11 is plotted in Fig. 4.12, which shows the intersection of the cylinder shown in Fig. 4.11. For the low contrast scatterers  $n_{\text{cyl}} = 1.001, 1.01$ , the reconstruction of the RI is closer to the ground truth RI for the FDT method than for the SSNP method. However, for the multiple scatterers  $n_{\text{cyl}} = 1.05$ , the SSNP method shows a better reconstruction of the RI than the FDT. This is in accordance with Fig. 4.11. The SSNP model is slightly off the ground truth solution for every cylinder, especially in the middle of the cylinder. A lower learning rate could improve this.

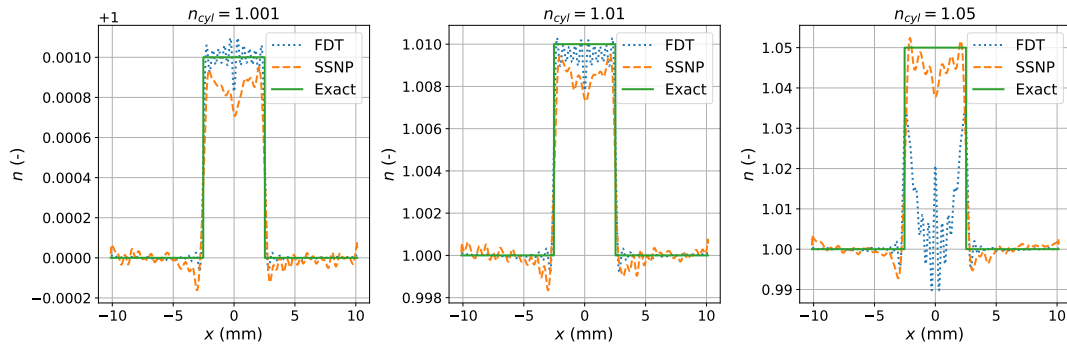


Figure 4.12: A intersection of the reconstruction of a cylinder with refractive index  $n_{\text{cyl}} = 1.001, 1.01, 1.05$  with the FDT and SSNP method. The reconstruction is computed with exact field data.

Since the computation time of an iterative solver depends on the number of iterations and the learning rate, a computation time analysis is performed on one iteration for different  $N_x = N_z$  such that the refractive index has a square domain. This computation time analysis is shown in Fig. 4.13 together with a linear ( $N_x$ ) and quadratic power law ( $N_x^2$ ) line, which are there for visualization purposes only. "gradient" refers to the computation time of the gradient computation and refractive index update, "loss" refers to the computation time of the loss with the current RI, the "setup" computation time is only performed ones for each projection and is the computation time for starting the SGD optimizer. The total computation time is referred to as "total". The most computation time is spent computing the gradient for each iteration, which significantly increases, even beyond the second order, for  $N_x \geq 2048$ . This could be due to cache misses since the arrays become bigger than the cache memory [33]. For  $N_x \leq 1024$ , the increase in time is about linear for each iteration.

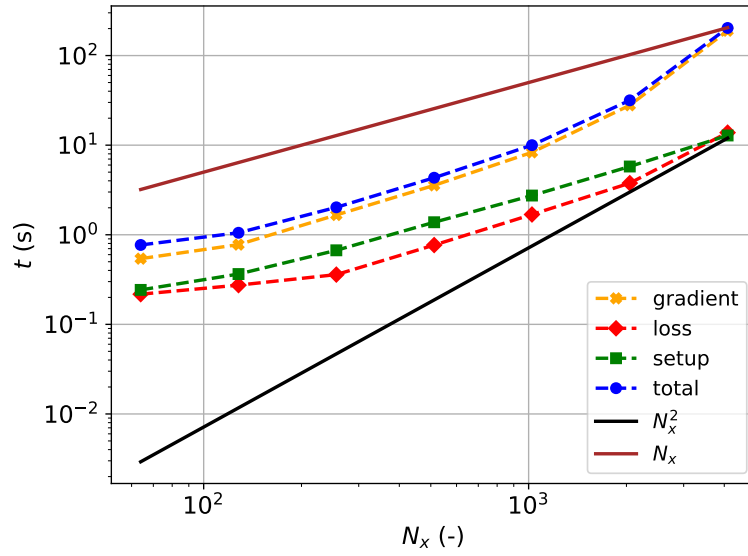


Figure 4.13: The computation time analysis for the reconstruction using the SSNP model on a log-log scale divided into the most computation time-consuming functions. The time is shown per iteration.

There is no general way to discuss the error for a certain amount of data points or steps in the  $z$ -direction since this depends on the learning rate and the number of iterations. To visualize this, Fig. 4.14 shows the computation of the refractive index for a cylinder with  $n_{\text{cyl}} = 1.001$ . Each refractive index is computed with a different learning rate  $\alpha = 0.02$  (left),  $\alpha = 0.2$  (middle), and  $\alpha = 2$  (right), but with the same maximum number of iterations: 200. The computation is performed on a square grid with  $N_x = N_z = 1024$ . The SSIM is highest for the middle figure with  $\alpha = 0.2$ . The lowest learning rate has not had enough iterations to compute the refractive index like the middle learning rate, and the highest learning rate misses details due to too big steps. The percentage error  $E$  is shown in Fig. 4.15 for an intersection in the middle of the refractive index domain. The error is the biggest at the boundary of the cylinder. The error is near zero in the areas outside the cylinder for both  $\alpha = 0.02, 0.2$ . However, for  $\alpha = 2$ , it oscillates a lot around zero in these regions. Inside the cylinder, the error is closest to 0 for  $\alpha = 0.2$ . There are more fluctuations for  $\alpha = 0.2$  than for  $\alpha = 0.02$ . For  $\alpha = 2$  inside the cylinder, there are still a lot of fluctuations.

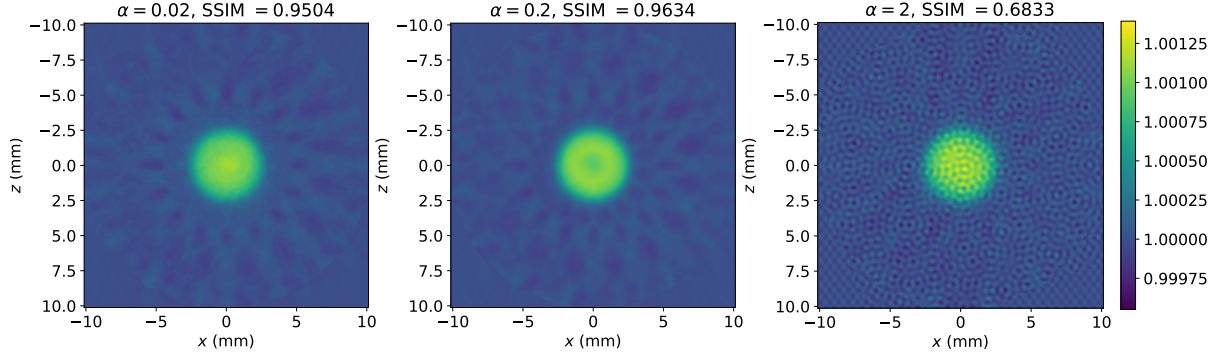


Figure 4.14: The reconstruction of the refractive index of a cylinder with  $n_{\text{cyl}} = 1.001$  using the SSNP model computed with three different learning rates  $\alpha = 0.02, 0.2, 2$ .

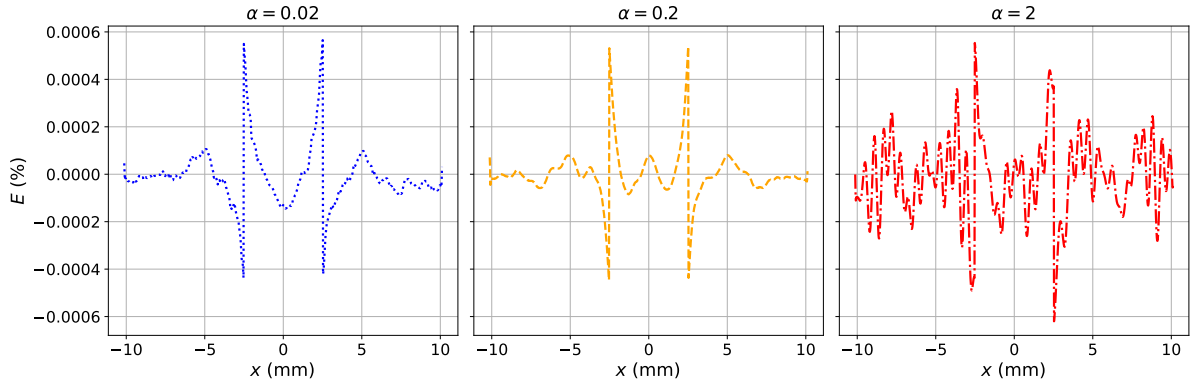


Figure 4.15: The percentage error  $E$  of an intersection of the refractive index computed with  $n_{\text{cyl}}$  for different learning rates ( $\alpha = 0.02, 0.2, 2$ ).

With the addition of the phase in the loss function in Eq. 3.2, calculating the derivative gets more complex. With this addition, the phase is also used for the reconstruction, which leads to extra data and the potential to reconstruct the RI more accurately. In the original SSNP paper by Zhu et al. [11], only the intensity is used to reconstruct the refractive index. A simulation is performed to see what this difference in the loss function leads to. With exactly the same parameters for both methods ( $\alpha = 20$ , max. iterations = 20,  $N_x = N_z = 2048$ ,  $n_{\text{cyl}} = 1.01$ ), the results differ significantly as can be seen in Fig. 4.16. Despite having the same parameters, the results are mirrored in  $n_m = 1$ , such that  $n_{\text{cyl}} = 1.01$  for the method from this thesis and  $n_{\text{cyl}} = 0.990$  for the SSNP method by Zhu et al.. The SSIM of the intensity-only method is higher than the SSIM of the method from this thesis. The intensity-only method converges to a mirrored solution in  $n_m = 1$  since the method misses phase information to reconstruct the RI.



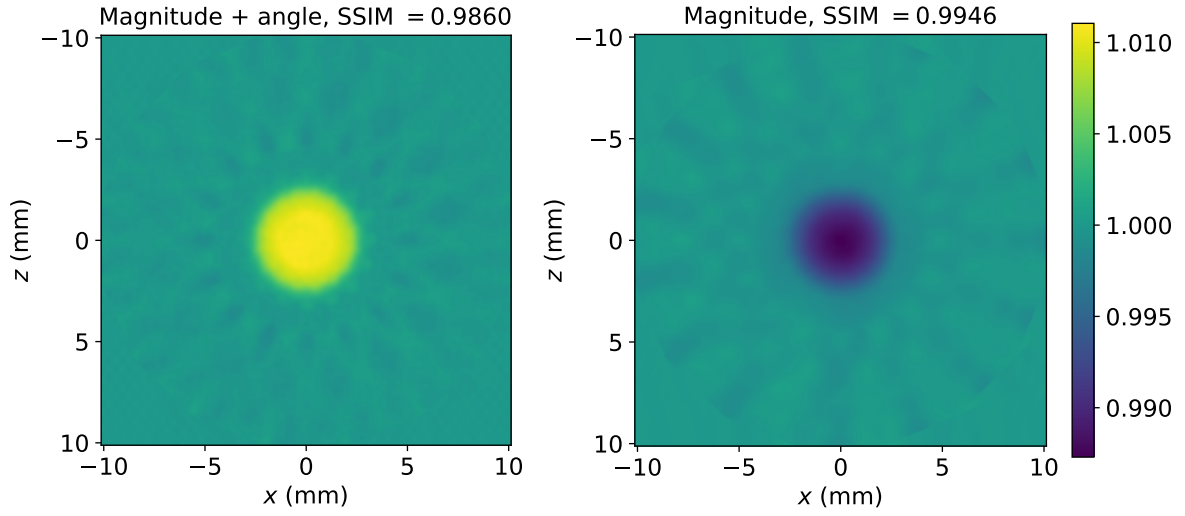


Figure 4.16: The refractive index obtained with the SSNP method from this thesis (left) and the paper by Zhu et al. (right) with exactly the same parameters. The ground truth solution is a cylinder with  $n_{\text{cyl}} = 1.01$ .

The percentage error  $E$  of an intersection for this figure is also shown in Fig. 4.17. The left figure shows the percentage error of the method from this thesis, which shows relatively small errors at the edges of the domain; however, the error is the biggest at the boundary of the cylinder. The middle figure shows the relative error for the SSNP method by Zhu et al.. This error is relatively big because the algorithm converges to a different solution. When computing the error with  $n_{\text{cyl}} = 0.990$ , which is shown in the right figure, the error decreases compared to the middle figure, and the pattern look like the error in the left figure only flipped.

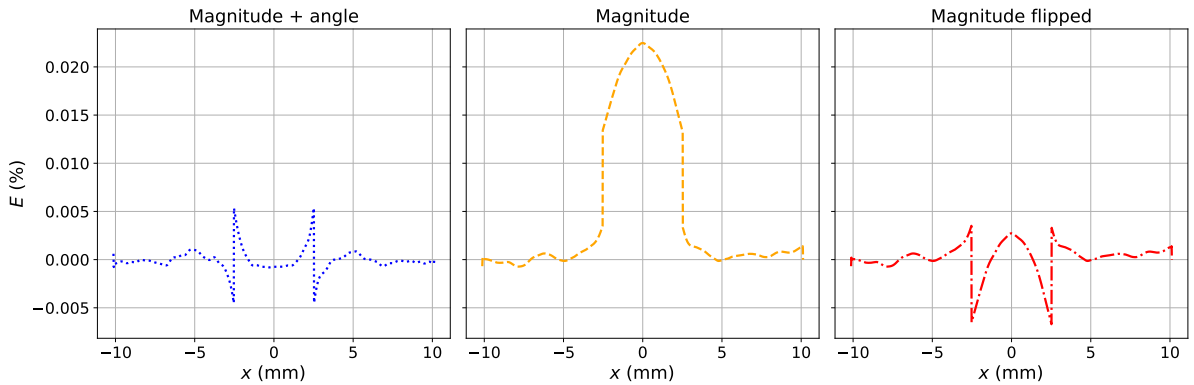


Figure 4.17: The percentage error  $E$  for an intersection of both the refractive index computed with the SSNP method from this thesis (left) and the SSNP method from Zhu et al. (middle) with exactly the same parameters. The right figure shows the error from Zhu's method with  $n_{\text{cyl}} = 0.990$ .

To speed up the code, another initial guess is used. Instead of the  $n(\mathbf{r}) = n_m$ , the solution of the FDT with object rotation is used as the estimated RI input for the SSNP model. In Table 4.1, the wall clock computation time is displayed for different  $n_{\text{cyl}}$  together with the learning rate and speed up. The maximum number of iterations is 100 and  $N_x = N_z = 2048$  for every  $n_{\text{cyl}}$ . For the low contrast scat-

ters  $n_{\text{cyl}} = 1.001$  and  $n_{\text{cyl}} = 1.01$ , the speed up is the biggest because fewer iterations are needed to reach the stopping criteria. Despite that the FDT using OR does not converge to the right solution for multiple scattering, which can be seen in Fig. 4.11, there is still a speed up because the edges of the cylinder are already roughly determined.

Table 4.1: The learning rate, time for the reconstruction with both the solution of the FDT method with OR ( $t_{\text{FDT}}$ ) and the background RI  $t_{n=n_m}$  as input, and the speed up for different values of  $n_{\text{cyl}}$ .

$n_{\text{cyl}}$	$\alpha$ (-)	$t_{\text{FDT}}$ (s)	$t_{n=n_m}$ (s)	Speed up (-)
1.001	1	1110	15040	13.5
1.01	5	3551	31260	8.8
1.05	25	26300	36301	1.4

As a proof of concept, two figures show the convergence for not-symmetrical refractive indices, such as the cylinder with an offset from the center in Fig. 4.18. The ground truth RI is shown in the left figure, and the reconstructed RI using the SSNP method is shown in the right figure. This RI is obtained with  $\alpha = 1$ , max. iterations = 100,  $N_\phi = 16$  and  $N_x = N_z = 2048$ . Figure 4.19 shows a more practical implementation, showing a phantom with an off-centered cell nucleus. The left figure again shows the ground truth RI and the right figure shows the reconstructed RI with the SSNP method. This tomographic RI is obtained with  $\alpha = 5$ , max. iterations = 20,  $N_\phi = 32$  and  $N_x = N_z = 2048$ . The blank areas originate from the *scipy.ndimage.rotate*-function, which sets the values of the new data points to the background RI  $n_m$ . This region is smaller for the reconstructed phantom since the angular step size is smaller.

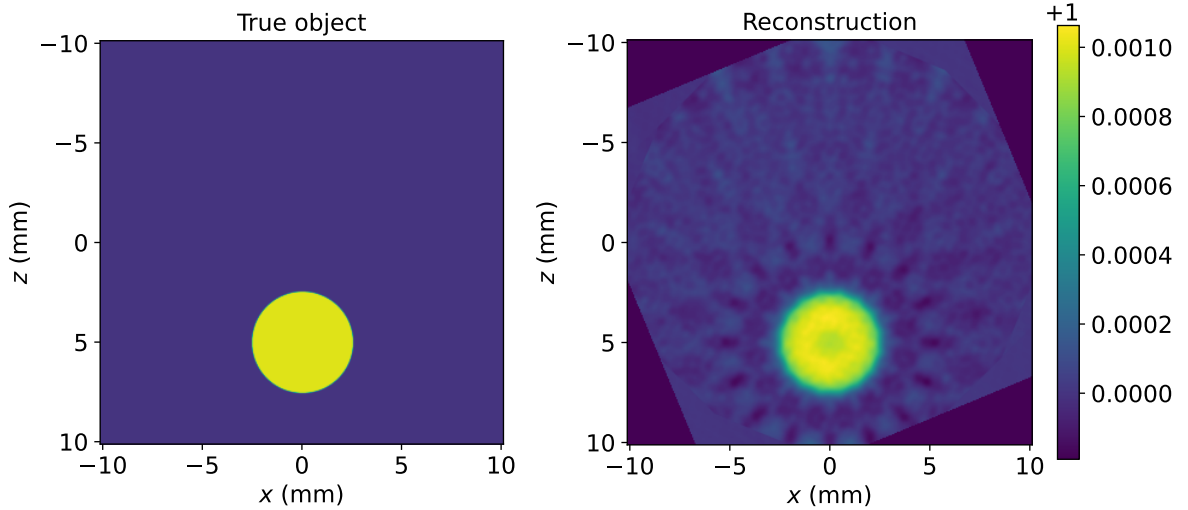


Figure 4.18: The reconstruction of an off-centered cylinder with left the ground truth RI and right the reconstructed RI obtained with the SSNP method. The used parameters are  $\alpha = 1$ , max. iterations = 100,  $N_\phi = 16$  and  $N_x = N_z = 2048$ .

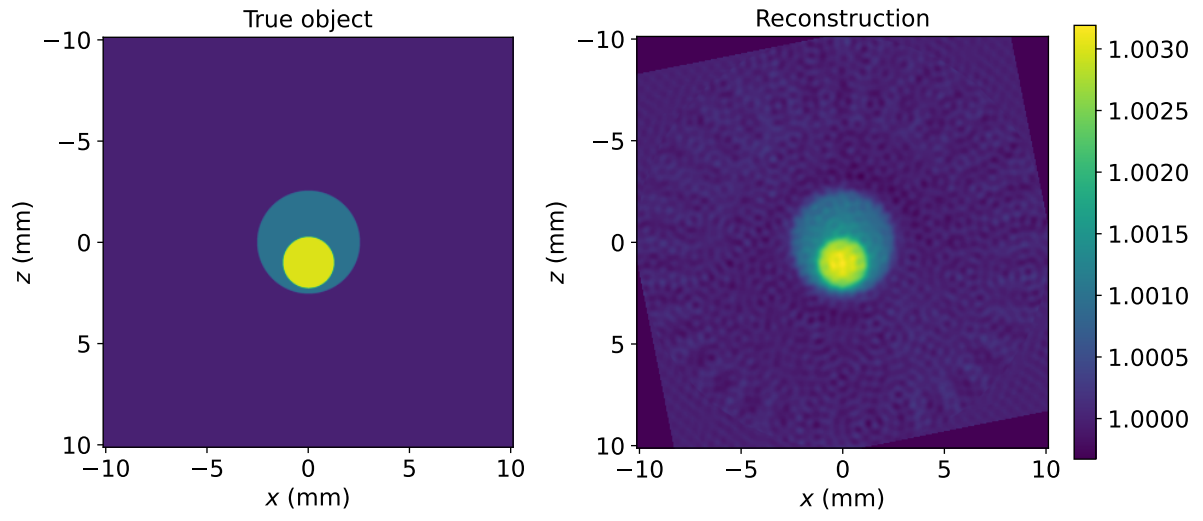


Figure 4.19: The reconstruction of a phantom with left the ground truth RI and right the reconstructed RI obtained with the SSNP method. The used parameters are  $\alpha = 5$ , max. iterations = 20,  $N_\phi = 32$  and  $N_x = N_z = 2048$ .

# 5

## Discussion

This chapter discusses the results presented in the previous chapter. This is done by examining the forward methods and suggesting recommendations to improve these methods. Secondly, the inverse methods and suggestions for future research are discussed.

### 5.1. The Forward Scattering Problem

The difference between the Born approximation and the exact field, both obtained with the Mie scattering theory, showed a decrease in the accuracy of the model when the refractive index of the cylinder increased. This increase in RMSE corresponds with the approximation made in the Born approximation. Only single scattering is accounted for in the Born approximation, meaning that as  $n_{\text{cyl}}$  increases, the difference increases since more multiple scattering takes place for a higher refractive index of the cylinder. Where the Born approximation showed a greater difference in magnitude as well as in the phase, in the Rytov approximation, this difference was mainly visible in the phase only. The difference in magnitude for the Rytov approximation was relatively small. This also resulted in a smaller RMSE. This is in agreement with the expectations since the Rytov approximation is generally more accurate [14]. The relatively small difference in phase between the Born and Rytov approximation can be explained by the fact that both approximations are based on the linearization of the wave equation. In this regime, the phase difference is typically small [34].

The SSNP forward model showed a solution close to the exact solution only with some ripples around the exact function and a phase close to the exact solution but with some deviations at the edges of the detector. The ripples cause the phase to be off at the edges of the detector, and they remain even when  $N_x$ ,  $N_z$  and  $n_{\text{cyl}}$  are increased. The ripples could be due to aliasing [35]. When the field is sampled at a lower sampling rate than its maximum frequency content, the higher frequency folds back into the lower frequency range. The low- and high-frequency components overlap, resulting in a distorted field representation. The error figures for the SSNP method followed the  $\mathcal{O}(\Delta z)$  introduced in the literature [15]. The stagnation of the curve could be due to the limiting precision of the used floats [36], however, more research is needed to validate this. The  $\mathcal{O}(\Delta x)$  convergence rate shows the same but stagnates faster. This suggests that the error is strongly determined by  $\Delta z$  since this stagnated value corresponds to the error obtained with the same  $\Delta z \approx 1.23$  nm. The convergence for decreasing  $n_{\text{cyl}}$  is also expected since for a higher refractive index, multiple scattering takes place, which results in a more accurate result when the scattering is obtained in smaller slices such that more multiple scattering gets used in the computation of the next slice. Since the error of  $\Delta z$  is linear  $\mathcal{O}(\Delta z)$ , the linear error for increasing  $n_{\text{cyl}}$  makes sense. To improve this forward model, a higher-order scheme could be used which would introduce a higher-order convergence rate, such as

the trapezoidal method, which has a  $\mathcal{O}((\Delta z)^2)$  convergence rate. However, this would increase the complexity of the model, even more, [37]. It is also recommended to test the convergence rates with more precision numbers such that the linear error  $\mathcal{O}(\Delta z)$  could be confirmed with the literature, even for the smallest step sizes.

## 5.2. The Inverse Problem

### 5.2.1. Fourier Refractive Index Reconstruction under the Born Approximation

The OR and LA methods showed convergence to the ground truth object using the Born field as input for these methods. The intersection in the  $x$ -direction matches the theory with a solution close to the ground truth object. Since more data points are used for the reconstruction with the LA method, the resolution is expected to improve with a maximum factor of 2 in this direction. In the  $z$ -direction, the LA method shows worse convergence which can be explained by the missing cone artifact. The interpolation is performed with data points further away, resulting in less accurate reconstructions in these areas. In contradiction to the OR method, the LA reconstruction is not  $n = 1$  outside of the cylinder. Instead, it fluctuates around  $n = 1$ , which could be explained because the data points are not close enough and therefore uses wrong values to reconstruct the data at the interpolation grid for the LA method. The reconstructed RI using the OR method is circularly symmetric, which is a direct consequence of scanning from every direction. The input data on every slice is the same for this method since the input RI is also circularly symmetric. Since the arcs are shifted differently for the LA method, the sampling grid covers the limited Ewald sphere, resulting in a resolution improved of a factor of 2. Therefore, more details could be captured by this method. In the OR method, only the Ewald sphere is covered.

The error study for increasing  $N_x$  showed higher accuracy for a low amount of data points for the LA method compared to the OR method. Due to the sampling, the Ewald sphere is more covered for the LA method, therefore, it yields more information and could yield a more accurate reconstruction. When  $N_x > 64$ , the OR method becomes more accurate than the LA because the effect of a more covered Ewald sphere is gone, and since the OR method does not have the missing cone effect, more relevant information is available for this method which then shows a more accurate reconstruction. The number of data points on the detector  $N_x$  needs to be sufficiently high to prevent aliasing from happening. Increasing  $N_x$ , increases the Nyquist frequency, resulting in a more accurate reconstruction since the highest captured frequency increases, resulting in fewer folded-back frequencies [38]. Therefore, the chances of aliasing are reduced for increased  $N_x$ . The number of angular projections  $N_\phi$  showed minimal effect on the RMSE for both methods and after  $N_\phi = 64$ , there is no increase in accuracy. This could be due to the *scipy.intp.griddata*-function, because this function uses linear Barycentric interpolation, which only uses the three closest points to compute the interpolation value. After  $N_\phi = 64$ , the three closest points do not change rigorously, and so the effect is minimal. The stagnation of the error could also be because the number of points on the detector  $N_x$  is the dominating factor for the error. The Crowther criterion suggests that for a certain resolution  $R$ , the minimum number of angular projections should be [39]

$$N_\phi = 2\pi R_0 R. \quad (5.1)$$

This criterion describes the trade-off between the radius of the cylinder  $R_0$  and the desired resolution. The increase in reconstruction accuracy for  $N_\phi \leq 64$  is expected by the Crowther criterion since the number of angular projections increases. Therefore, the resolution increases too, resulting in a more accurate reconstruction.

The computation time figures showed that the *scipy.intp.griddata*-function is the most time-consuming

function for both methods. This function uses Delaunay triangulation and linear Barycentric interpolation, which has  $\mathcal{O}(N \log N)$  and  $\mathcal{O}(M)$  for  $N$  the number of points on the sample grid and  $M$  the number of points on the interpolation grid. Therefore, if  $N_x$  increases, both  $N$  and  $M$  increase squared, which enlarges the computational complexity. Since LA uses a bigger grid to interpolate on, especially for fewer data points, LA reconstruction is expected to be slower for every  $N_x$ . The bigger interpolation grid is a direct consequence of a potentially twice as wide  $k_x$ -range. The results showed that the OR method is slower for most data points, which is unexpected because the interpolation grid is bigger due to a wider sampling of the data points. For  $N_x \geq 1024$ , the LA method is slower, which is expected. For all  $N_\phi$ , OR reconstruction is more time-consuming than LA. This is not expected since the interpolation grid is bigger for LA. However, it could be due to the bigger spacing of the sample grid for the LA method, leaving more space between sample points. Performing the Delaunay triangulation for a bigger sampling spacing is less computationally complex [40].

Modifying the *scipy.intp.griddata*-function is recommended as it is computationally the most time-consuming step in both methods. This function becomes even more constraining if this code is implemented in 3D since the grid becomes  $N_x$  times bigger. To speed up the *scipy.intp.griddata*-function, all the filtered out ( $k_x^2 < k_m^2$ ) information could be left out of the interpolation to make the sample grid smaller, especially for large  $N_x$ . It is also possible to perform the Delaunay triangulation once for every combination of  $N_x$  and  $N_\phi$ . This will make the *scipy.intp.griddata*-function more effectively since the triangulation only needs to be performed once [22]. This will speed up the code when performing several tests with the same parameters. Other interpolation methods could improve the reconstruction accuracy, such as the Radial Basis Function Interpolation Method [41].

### 5.2.2. Iterative Reconstruction with the SSNP Model

Where the FDT method did not converge to the ground truth object for  $n_{\text{cyl}} = 1.05$ , the inverse SSNP model did converge for all shown values of  $n_{\text{cyl}}$ . This shows the expected results for FDT and SSNP. It is predicted that a high refractive index would lead to big errors for the FDT method and that the SSNP would converge for every refractive index if  $N_x$  and  $N_z$  are sufficiently high. The intersection of the reconstructed RI showed that there was a small deviation in the middle of the cylinder for the SSNP method. A lower learning rate and more iterations for the SSNP method could improve this. However, this will lead to an even higher computation time. The errors of the refractive indices are the biggest at the boundary of the cylinder for every method. This makes sense because the refractive index of the cylinder is not smooth, which makes it more complex to reconstruct it exactly. The same results for multiple scattering are obtained in the work of Lim et al. [16], where the reconstruction is close to the ground truth object, except for the boundaries, where a small deviation is visible.

The computation time analysis of the SSNP model showed that the gradient computation by *TensorFlow* is the most computation time-consuming part of the tomographic reconstruction for each iteration. This is expected since it is a sequential method with  $N_z$  slices computed slice-by-slice. So computing the derivative is a complex function consisting of a for-loop and  $(4N_z + 2)$  Fourier transforms. To improve this algorithm, a learning algorithm could be used in *TensorFlow*, which could compute the gradient faster and reduce each iteration's computational complexity. Furthermore, the implementation could be changed to reduce the amount of Fourier transforms. The matrix  $\mathbf{P}$  and  $\mathbf{Q}$  commute since they originate from a sum in an exponential function. Matrix  $\mathbf{P}$  is computed in the Fourier domain, and matrix  $\mathbf{Q}$  in real space. To reduce the amount of FFT, the order of computation could be changed to

$$U_{\text{for}} = \mathbf{F}\mathbf{P}\mathbf{Q}(z_{n-1}) \cdots \mathbf{P}\mathbf{Q}(z_1)\mathbf{Q}(z_0)\mathbf{P}\Phi_0, \quad (5.2)$$

which results in approximately half the amount of Fourier transforms and, therefore, a decrease in computation time.

The accuracy of the SSNP method is hard to determine for different values since a change of parameters could lead to a different optimal learning rate. However, it is good to understand the convergence for different learning rates with the same maximum number of iterations. It is expected that the lower the learning rate, the more accurate the results, but if the maximum number of iterations is too low, it converges too slowly. Therefore, the error could still be higher than for a higher learning rate. The learning rate  $\alpha = 0.2$  showed the best convergence even though the reconstruction was also performed with a lower learning rate. For an even higher learning rate, it is shown that the results are more off even in the regions outside of the cylinder. This could be due to the missing information due to a too-big step. It is recommended to perform an extensive study for the best combinations of the maximum number of iterations, learning rates, and computation time until converging.

With the SSNP method introduced in this thesis, the reconstruction includes the phase when computing the error instead of only the intensity. This extra used data was also visible in the reconstruction tests between the intensity and phase vs. the intensity only. With the same parameters, they converged to two different solutions. Due to the extra information originating from the phase, the reconstruction accuracy improved. Since this is only tested in one situation, studying the performance of both solvers with multiple refractive indices is recommended. In Lim et al. [16], the phase and intensity are included for the reconstruction. Since the accuracy also depends on the learning rate and the maximum number of iterations, it is hard to tell which method is more accurate from these refractive indices. However, compared to the introduced method in this thesis, the reconstruction of a cylinder with a homogeneous RI showed similar reconstructions where the error is the biggest at the cylinder's edge. With the introduced method, the intensity gets more value in the loss function in Eq. 3.2. This is because the forward SSNP method is generally more accurate for the field's intensity than for the field's phase.

The new input refractive index from the FDT method showed a speed up with a maximum of 13.5 for the computation of the refractive index compared to the background RI as input. This speed up is mostly because fewer iterations are needed. Therefore the speed up decreases for highly scattering objects because the reconstruction of the FDT method is worse for these scatterers. The speed up of 1.4 for multiple scatterers is still huge for a computation that could take hours.

The two proofs of concepts with the off-centered cylinder and the phantom showed the potential of the SSNP method. It can reconstruct more complex refractive indices, which can even be multiple scatterers. Therefore, this implementation will be even more flexible than the FDT method. The biggest downside of the current implementation of the SSNP method is that it is computationally time-consuming. A learning algorithm could be used to speed up the current implementation as discussed in Lim et al. [16]. Next to implementing a learning algorithm to speed up the gradient, a different optimizer could be used, such as the adaptive moment estimation (Adam) optimizer. With the correct parameters, the Adam optimizer is always faster and more accurate than the currently used SGD optimizer [42]. This method updates the learning rate based on exponential decay rates. With the right exponential decay rates, the solver could need fewer iterations because, first, a rough guess of the RI is taken, after which lower learning rates are used to update this guess more refined.

For future research, it is recommended to speed up the current SSNP reconstruction so that it becomes more practical to use by implementing the mentioned improvements, it is recommended to implement the theory of 3D reconstruction so that more realistic objects can be reconstructed, and it is recommended to implement the illumination scanning reconstruction with the SSNP method. Figure A.1 in the appendix showed that the FDT allows for reconstructing complex-valued refractive

indices. This is also possible for the SSNP model by implementing a complex refractive index and a complex derivative. It is recommended to implement this such that more realistic objects can be reconstructed with the SSNP model.



# 6

## Conclusion

For the imaging of biological cells, the most optimal imaging techniques are needed to study human diseases. In this thesis, a quantitative study is conducted to investigate optical diffraction tomography in various forms. First, the Mie scattering and split step non-paraxial (SSNP) methods are used to compute the complex field at a detector. This data is then used for the reconstruction of the refractive index (RI) of an object. The reconstruction is done with variants of the Fourier diffraction theorem (FDT): the sample rotation (OR) and the illumination scanning (LA) method. Additionally, the RI is also reconstructed with the SSNP reconstruction method using sample rotation.

The FDT uses the Born approximation of the scattered field; therefore, the reconstruction is only valid for single scatterers. The RI can be obtained by sampling the data from the detector on semi-circular arcs, interpolating the data on a Cartesian grid, and performing a 2D inverse Fourier Transform. The SSNP reconstruction method is implemented by iteratively updating the RI by computing the gradient using automatic differentiation in the *TensorFlow*-package. This method is valid for every scatterer, but since the field is computed sequentially, the method is time-consuming. All the simulations are done on a cylinder with a constant refractive index in a constant homogeneous background refractive index.

The Mie scattering models showed expected behavior with decreased accuracy of the complex field for increasing the refractive index of the cylinder between the Born and Rytov approximation, with the field computed with the Rytov approximation structural a lower error. The forward SSNP model showed first-order convergence for the step size in the  $z$ -direction  $\mathcal{O}(\Delta z)$ . This is in accordance with the literature. The error is also dependent on the step size in the  $x$ -direction, however, the error is dominated by  $\Delta z$ .

The OR and LA reconstruction using FDT showed convergence for all refractive indices when using the Born field. The LA method showed better performance for a small number of detector points,  $N_x \leq 64$ , but this performance is passed by the OR method for higher  $N_x$ . The most time-consuming function for both methods is the *scipy.intp.griddata*-function due to the Delaunay triangulation and the linear Barycentric method.

The reconstruction with the SSNP method showed convergence for all refractive indices in contradiction to the FDT method with the exact field using sample rotation. The gradient computation took the most computation time, which makes sense because it is the derivative of a sequential algorithm. The implementation using both the phase and intensity showed better convergence than the intensity only, because the intensity converged to a different solution. The best performance of the SSNP

implementation is reached with the OR reconstruction data as input, even for multiple scatterers, since fewer iterations are needed before reaching the stopping criteria.

It is recommended to improve the FDT method by only using the data points which are not filtered out ( $k_x^2 < k_m^2$ ) such that the sample and interpolation grid sizes are decreased and, therefore, the computation time. Furthermore, the SSNP method can be improved by applying a learning algorithm that could improve code performance and, for a more versatile code, a 3D implementation of all shown methods is recommended. Implementing a reconstruction algorithm for a complex-valued RI and implementing the illumination scanning method with the SSNP model is also recommended to make the model suitable for more realistic objects.

# Bibliography

- [1] KyeoReh Lee, Kyoohyun Kim, Jaehwang Jung, JiHan Heo, Sangyeon Cho, Sangyun Lee, Gyuyoung Chang, YoungJu Jo, Hyunjoo Park, and YongKeun Park. Quantitative phase imaging techniques for the study of cell pathophysiology: From principles to applications. *Sensors*, 13(4):4170–4191, 2013.
- [2] U.S. Food and Drug Administration. Medical X-Ray Imaging. <https://www.fda.gov/radiation-emitting-products/medical-imaging/medical-x-ray-imaging>, 2021. Accessed: June 26, 2023.
- [3] National Center for Biotechnology Information. Medical Imaging. <https://www.ncbi.nlm.nih.gov/books/NBK564362/>, 2022. Accessed: June 26, 2023.
- [4] Arkadiusz Kuś, Wojciech Krauze, Piotr L Makowski, and Małgorzata Kujawińska. Holographic tomography: hardware and software solutions for 3d quantitative biomedical imaging. *Etri Journal*, 41(1):61–72, 2019.
- [5] Eugene Lin and Adam Alessio. What are the basic concepts of temporal, contrast, and spatial resolution in cardiac CT? <https://www.ncbi.nlm.nih.gov/pmc/articles/PMC4752333/#:~:text=Current%20CT%20scanners%20have%20a,x%2D%20to%20y%2Daxes.,2009>, 2009.
- [6] Kyoohyun Kim, Jonghee Yoon, Seungwoo Shin, Lee Sangyun, Su-A Yang, and YongKeun Park. Optical diffraction tomography techniques for the study of cell pathophysiology. *Journal of Biomedical Photonics & Engineering*, 2, 03 2016.
- [7] Max Planck Institute for the Science of Light, Guck Division. Phase imaging and tomography. Retrieved from <https://mpl.mpg.de/divisions/guck-division/methods/phase-imaging-and-tomography>, n.d.
- [8] P. Müller. *Optical Diffraction Tomography for Single Cells*. Phd thesis, Technischen Universit Dresden, 2016.
- [9] Chansuk Park, Seungwoo Shin, and YongKeun Park. Generalized quantification of three-dimensional resolution in optical diffraction tomography using the projection of maximal spatial bandwidths. *J. Opt. Soc. Am. A*, 35(11):1891–1898, Nov 2018.
- [10] Paul Müller, Mirjam Schürmann, and Jochen Guck. The theory of diffraction tomography, 2016.
- [11] Jiabei Zhu, Hao Wang, and Lei Tian. High-fidelity intensity diffraction tomography with a non-paraxial multiple-scattering model. *Opt. Express*, 30(18):32808–32821, Aug 2022.
- [12] Jaebum Lim, KyeoReh Lee, Kyong Hwan Jin, SeoEun Shin, Sangyeop Lee, YongKeun Park, and Jong Chul Ye. Comparative study of iterative reconstruction algorithms for missing cone problems in optical diffraction tomography. *Optics Express*, 23(13):16933–16948, 2015.
- [13] P.Y. Liu, Lip Ket Chin, Wee Ser, Hongfu Chen, C.-M Hsieh, C.-H Lee, Kung-Bin Sung, Teck Ayi, Peng Yap, Bo Liedberg, Kuan Wang, T. Bourouina, and Yamin Leprince-Wang. Cell refractive index for cell biology and disease diagnosis: Past, present and future. *Lab on a chip*, 16, 01 2016.

- [14] Anthony J. Devaney. *Mathematical Foundations of Imaging, Tomography and Wavefield Inversion*. Cambridge University Press, 2012.
- [15] Jiabei Zhu, Hao Wang, and Lei Tian. Supplementary document for High-fidelity intensity diffraction tomography with a non-paraxial multiple-scattering model - 5994472.pdf. 8 2022.
- [16] Joowon Lim, Ahmed B. Ayoub, Elizabeth E. Antoine, and Demetri Psaltis. High-fidelity optical diffraction tomography of multiple scattering samples. *Light: Science & Applications*, 8(1):82, 09 2019.
- [17] C. Linton. The green’s function for the two-dimensional helmholtz equation in periodic domains. *Journal of Engineering Mathematics*, 33:377–401, 01 1998.
- [18] Raimi Karim. Intuitions on l1 and l2 regularisation. <https://towardsdatascience.com/intuitions-on-l1-and-l2-regularisation-235f2db4c261>, Oct 2020.
- [19] Ulugbek S. Kamilov, Ioannis N. Papadopoulos, Morteza H. Shoreh, Alexandre Goy, Cedric Vonesch, Michael Unser, and Demetri Psaltis. Optical tomographic image reconstruction based on beam propagation and sparse regularization. *IEEE Transactions on Computational Imaging*, 2(1):59–70, 2016.
- [20] Guido Van Rossum and Fred L. Drake. *Python 3 Reference Manual*. CreateSpace, Scotts Valley, CA, 2009.
- [21] Intel. Intel® core™ i7-9750h processor. Intel® ARK (Product Specifications), 2019. <https://ark.intel.com/content/www/us/en/ark/products/191045/intel-core-i79750h-processor-12m-cache-up-to-4-50-ghz.html>.
- [22] Pauli Virtanen, Ralf Gommers, Travis E. Oliphant, Matt Haberland, Tyler Reddy, David Cournapeau, Evgeni Burovski, Pearu Peterson, Warren Weckesser, Jonathan Bright, Stéfan J. van der Walt, Matthew Brett, Joshua Wilson, K. Jarrod Millman, Nikolay Mayorov, Andrew R. J. Nelson, Eric Jones, Robert Kern, Eric Larson, C J Carey, İlhan Polat, Yu Feng, Eric W. Moore, Jake VanderPlas, Denis Laxalde, Josef Perktold, Robert Cimrman, Ian Henriksen, E. A. Quintero, Charles R. Harris, Anne M. Archibald, Antônio H. Ribeiro, Fabian Pedregosa, Paul van Mulbregt, and SciPy 1.0 Contributors. SciPy 1.0: Fundamental Algorithms for Scientific Computing in Python. *Nature Methods*, 17:261–272, 2020.
- [23] Charles R. Harris, K. Jarrod Millman, Stéfan J. van der Walt, Ralf Gommers, Pauli Virtanen, David Cournapeau, Eric Wieser, Julian Taylor, Sebastian Berg, Nathaniel J. Smith, Robert Kern, Matti Picus, Stephan Hoyer, Marten H. van Kerkwijk, Matthew Brett, Allan Haldane, Jaime Fernández del Río, Mark Wiebe, Pearu Peterson, Pierre Gérard-Marchant, Kevin Sheppard, Tyler Reddy, Warren Weckesser, Hameer Abbasi, Christoph Gohlke, and Travis E. Oliphant. Array programming with NumPy. *Nature*, 585(7825):357–362, September 2020.
- [24] James W. Cooley and John W. Tukey. An algorithm for the machine calculation of complex fourier series. *Mathematics of Computation*, 19(90):297–301, 1965.
- [25] D. T. Lee and B. J. Schachter. Two algorithms for constructing a delaunay triangulation. *International Journal of Computer & Information Sciences*, 9(3):219–242, Jun 1980.
- [26] Kai Hormann. Barycentric interpolation. In Gregory E. Fasshauer and Larry L. Schumaker, editors, *Approximation Theory XIV: San Antonio 2013*, pages 197–218, Cham, 2014. Springer International Publishing.

- [27] Martín Abadi, Ashish Agarwal, Paul Barham, Eugene Brevdo, Zhifeng Chen, Craig Citro, Greg S. Corrado, Andy Davis, Jeffrey Dean, Matthieu Devin, Sanjay Ghemawat, Ian Goodfellow, Andrew Harp, Geoffrey Irving, Michael Isard, Yangqing Jia, Rafal Jozefowicz, Lukasz Kaiser, Manjunath Kudlur, Josh Levenberg, Dandelion Mané, Rajat Monga, Sherry Moore, Derek Murray, Chris Olah, Mike Schuster, Jonathon Shlens, Benoit Steiner, Ilya Sutskever, Kunal Talwar, Paul Tucker, Vincent Vanhoucke, Vijay Vasudevan, Fernanda Viégas, Oriol Vinyals, Pete Warden, Martin Wattenberg, Martin Wicke, Yuan Yu, and Xiaoqiang Zheng. TensorFlow: Large-scale machine learning on heterogeneous systems, 2015. Software available from tensorflow.org.
- [28] Chi-Feng Wang. Automatic differentiation, explained. <https://towardsdatascience.com/automatic-differentiation-explained-b4ba8e60c2ad>, Mar 2019.
- [29] James A. Badner. Param user guide. <https://param.holoviz.org/>, journal=Welcome to Param! - param v1.13.0, Mar 2023.
- [30] Robert Gilmore Pontius, Olufunmilayo Thontteh, and Hao Chen. Components of information for multiple resolution comparison between maps that share a real variable. *Environmental and Ecological Statistics*, 15(2):111–142, June 2008.
- [31] Zhou Wang, A.C. Bovik, H.R. Sheikh, and E.P. Simoncelli. Image quality assessment: from error visibility to structural similarity. *IEEE Transactions on Image Processing*, 13(4):600–612, 2004.
- [32] Emmanuelle Gouillart. Structural similarity index. [https://scikit-image.org/docs/dev/auto\\_examples/transform/plot\\_ssim.html](https://scikit-image.org/docs/dev/auto_examples/transform/plot_ssim.html), 2023.
- [33] Rajkumar Upadhyay. Types of cache misses. <https://www.geeksforgeeks.org/types-of-cache-misses/>, May 2023.
- [34] Avinash C Kak and Malcolm Slaney. *Principles of computerized tomographic imaging*. SIAM, 2001.
- [35] David G Voelz. *Computational fourier optics: a MATLAB tutorial*. SPIE, 2011.
- [36] Milan Klöwer, Sam Hatfield, Matteo Croci, Peter Düben, and Tim Palmer. Fluid simulations accelerated with 16 bits: Approaching 4x speedup on a64fx by squeezing shallowwaters.jl into float16. *Journal of Advances in Modeling Earth Systems*, 14, 02 2022.
- [37] J. van Kan, A. Segal, F. Vermolen, and H. Kraaijevanger. *Numerical Methods for Partial Differential Equations*. DAP, 2019.
- [38] John W Leis. *Digital signal processing using MATLAB for students and researchers*. John Wiley & Sons, 2011.
- [39] Richard Anthony Crowther, DJ DeRosier, and Aaron Klug. The reconstruction of a three-dimensional structure from projections and its application to electron microscopy. *Proceedings of the Royal Society of London. A. Mathematical and Physical Sciences*, 317(1530):319–340, 1970.
- [40] D.T. Lee and B.J. Schachter. Two algorithms for constructing a delaunay triangulation. *International Journal of Computer and Information Sciences*, 9:219–242, 1980.
- [41] Chin-Shung Yang, Szu-Pyng Kao, Fen-Bin Lee, and Pen-Shan Hung. Twelve different interpolation methods: A case study of surfer 8.0. *Journal of Geographic Information and Decision Analysis*, 2019.

- [42] Geek Culture. A 2021 guide to improving CNNs: Optimizers - Adam vs SGD. *Medium*, March 2021.
- [43] Milton Abramowitz, Irene A Stegun, and Robert H Romer. *Handbook of mathematical functions with formulas, graphs, and mathematical tables*. American Association of Physics Teachers, 1988.

# A

## Appendix

The implementation of a complex-valued refractive index is shown in Fig. A.1 reconstructed with the OR method and the Born field as input. The refractive index of the cylinder is set to be  $n_{\text{cyl}} = 1.01 + 0.005i$ . The real parts of the RI are shown in the left figure, where the RI is corrected with  $-1$  such that the real part of the refractive index is of the same order as the imaginary part. The right figure shows the imaginary part. The reconstruction converges to the ground truth solution, so the FDT works for complex refractive indices. The results are obtained with  $N_x = 1024$ .

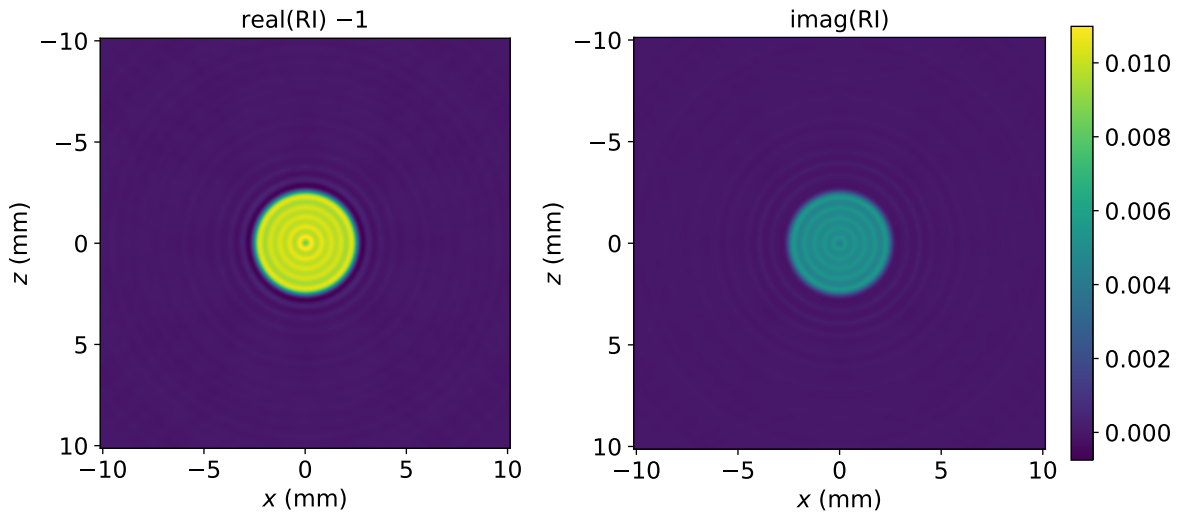


Figure A.1: The reconstruction of a cylinder with a complex-valued refractive index  $n_{\text{cyl}} = 1.01 + 0.005i$ . The left figure shows the real refractive index minus 1, and the right figure shows the complex refractive index.

The absolute value of the sinogram computed with the Born field is shown in the left figure of Fig. A.2 for the OR method and of Fig. A.3 for the LA method. The OR method shows the same field for every  $N_\phi$  because the object is circularly symmetric, and for the sample rotation, the input angle does not change then. The LA method shows a different sinogram where the effect of the input angle can be seen. When changing the input angle to the maximum angle  $\phi_{\text{max}} = 0.45\pi$ , the field at the edge of the detector becomes stronger because then the field propagates through the cylinder from a further

angle resulting in a shift of the peak of the complex field. The same shape is reached for the angles around  $\phi = 0$  as the OR method. This makes sense because then the input angle is about the same.

The absolute value of the fast Fourier transform of the sinogram is shown in Fig. A.2 for the OR method and in Fig. A.3 for the LA method on the right. The Fourier transform narrows the pattern for both methods, which is expected since both methods have approximately a Gaussian function of which the Fourier transform is again a Gaussian function, but narrower [43].

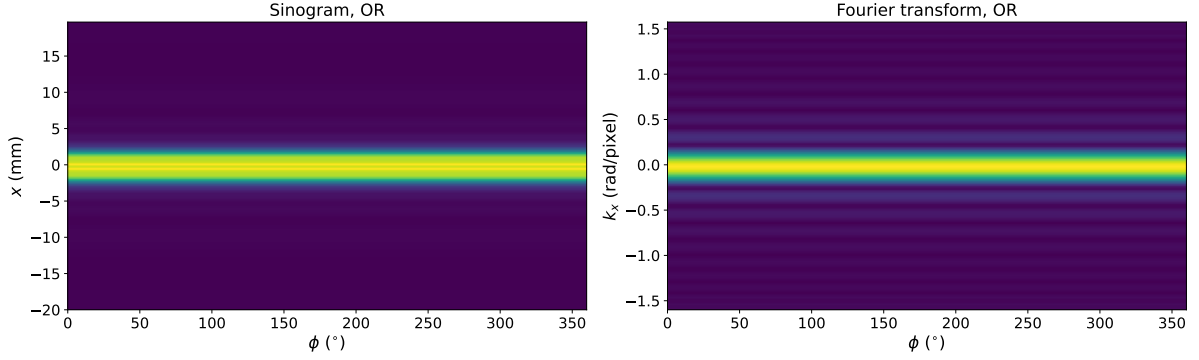


Figure A.2: The absolute value of the sinogram (left) obtained with the Born approximation and the absolute value of the FFT (right) for the OR method.

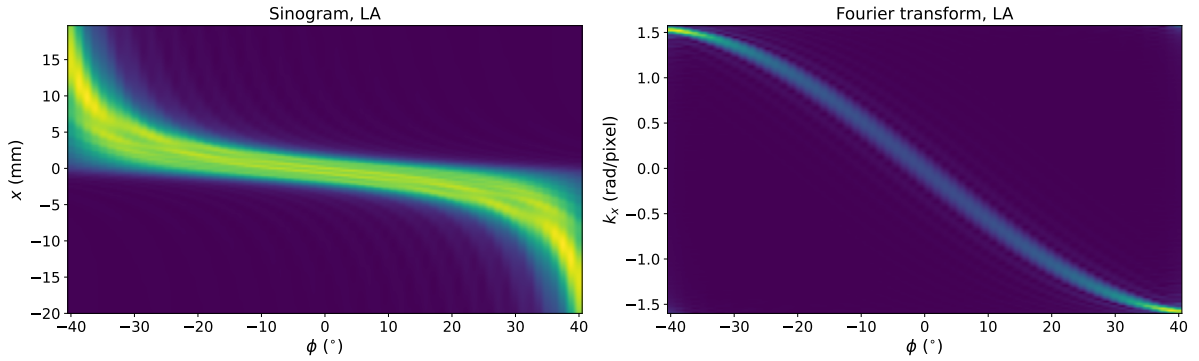


Figure A.3: The absolute value of the sinogram (left) obtained with the Born approximation and the absolute value of the FFT (right) for the LA method.

The percentage error of the reconstructed RI computed with FDT and SSNP methods is shown in Fig. A.4. This figure is an addition to Fig. 4.11 where the RI is shown for the same solvers and  $n_{\text{cyl}}$ . The error is relatively small for  $n_{\text{cyl}} = 1.001, 1.01$ , because these are low contrast scatterers, and the Born approximation is therefore valid. The biggest error is then for the cylinder's edge since the refractive index is not continuous. The RI of the cylinder  $n_{\text{cyl}} = 1.05$  showed the biggest error for the FDT method since the exact solution is no longer close to the ground truth solution, as seen in Figs. 4.1-4.2. The SSNP method showed convergence for every  $n_{\text{cyl}}$  since this method does not assume low contrast scattering. However, this method still shows an error at the cylinder's edge for the same reason as the FDT method.



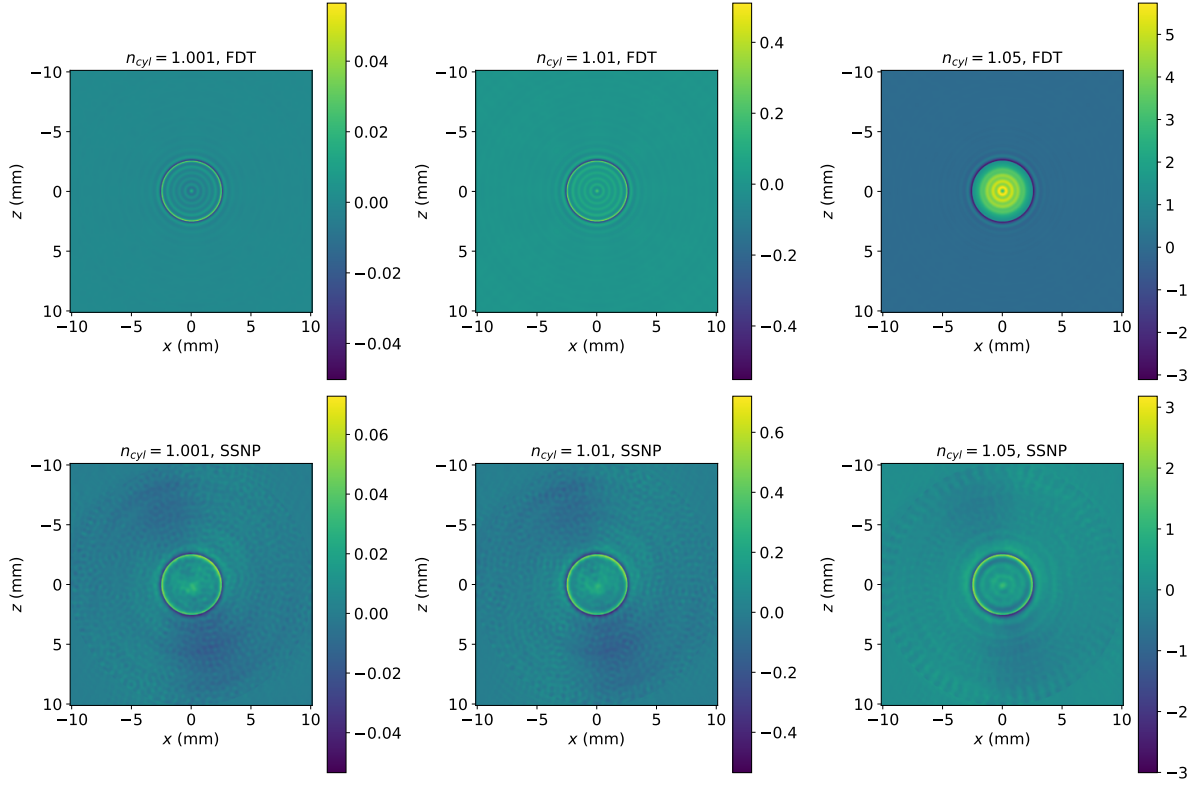


Figure A.4: The percentage difference of the RI computed with the FDT and SSNP methods as an addition for Fig. 4.11.